Geophysical Prospecting EAGE EUROPEAN ASSOCIATION OF GEOSCIENTISTS & ENGINEERS

Geophysical Prospecting, 2015, **63**, 774–797 doi: 10.1111/1365-2478.12238

Delineating structures controlling sandstone-hosted base-metal deposits using high-resolution multicomponent seismic and radio-magnetotelluric methods: a case study from Northern Sweden

Alireza Malehmir[1]*, Shunguo Wang[1], Jarkko Lamminen[2], Bojan Brodic[1], Mehrdad Bastani[3], Katri Vaittinen[2], Christopher Juhlin[1] and Joachim Place[1]

[1]*Department of Earth Sciences, Uppsala University, Villavägen 16, SE 75236, Uppsala, Sweden,* [2]*Boliden Mineral AB, Kontorsvägen 1, Boliden, SE 93681, Sweden, and* [3]*Geological Survey of Sweden, Box 670, SE 75128, Uppsala, Sweden*

Received September 2014, revision accepted December 2014

ABSTRACT

Over the past few decades seismic methods have increasingly been used for the exploration of mineral, geothermal, and groundwater resources. Nevertheless, there have only been a few cases demonstrating the advantages of multicomponent seismic data for these purposes. To illustrate some of the benefits of three-component data, a test seismic survey, using 60 digital three-component sensors spaced between 2 m and 4 m and assembled in a 160 m-long prototype landstreamer, was carried out over shallow basement structures underlying mineralized horizons and over a magnetic lineament of unknown origin. Two different types of seismic sources, i.e., explosives and a sledgehammer, were used to survey an approximately 4 km-long seismic profile. Radio-magnetotelluric measurements were also carried out to provide constraints on the interpretation of the seismic data over a portion of the profile where explosive sources were used. Good quality seismic data were recorded on all three components, particularly when explosives were used as the seismic source. The vertical component data from the explosive sources image the top of the crystalline basement and its undulated/faulted surface at a depth of about 50 m–60 m. Supported by the radio-magnetotelluric results, however, shallower reflections are observed in the horizontal component data, one of them steeply dipping and associated with the magnetic lineament. The vertical component sledgehammer data also clearly image the crystalline basement and its undulations, but significant shear-wave signals are not present on the horizontal components. This study demonstrates that multicomponent seismic data can particularly be useful for providing information on shallow structures and in aiding mineral exploration where structural control on the mineralization is expected.

Key words: Hard rock environment, Multicomponent, Landstreamer, Radio-magnetotelluric, Mineral exploration, Fault, Basement.

1 INTRODUCTION

From a number of case studies recently presented in the literature (e.g., Milkereit *et al.* 1996, 2000; Eaton 1999; Pretorius *et al.* 2000; White *et al.* 2000; White, Secord, and Malinowski 2012; Adam *et al.* 2003; Greenhalgh, Zhou, and Cao 2003; Gillot *et al.* 2005; Eaton *et al.* 2010; Hajnal *et al.* 2010; Cheraghi, Malehmir, and Bellefleur 2012; Dehghannejad *et al.* 2010, 2012; Ehsan, Malehmir, and Dehghannejad 2012; Koivisto *et al.* 2012; Juhojuntti *et al.* 2012; Malinowski,

*E-mail: alireza.malehmir@geo.uu.se

Schetselaar, and White 2012; Malehmir and Bellefleur 2009; Malehmir *et al.* 2009, 2011, 2012a,b, 2014; Manzi *et al.* 2012a,b; Urosevic *et al.* 2012; Ahmadi *et al.* 2013; Hurich and Deemer 2013), it is evident that seismic methods are increasingly being used for mineral, geothermal, and groundwater exploration. Nevertheless, only a few attempts and studies have been carried out to illustrate the value of multicomponent seismic methods for these purposes (Bohlen, Müller, and Milkereit 2003; Bellefleur *et al.* 2004; Bellefleur, Malehmir, and Müller 2012; Snyder, Cary, and Salisbury 2008; Malinowski and White 2011; White *et al.* 2012). Most mineral deposits, particularly the metallic ones, show a significantly higher S-wave than P-wave velocity contrast with their host rocks (Salisbury, Harvey, and Matthews 2003; Duff *et al.* 2012; Malehmir *et al.* 2013b). In addition, S-wave data can provide information about anisotropy and physical properties (Thomsen 1999; Stewart *et al.* 2002, 2003), useful for both exploration and mine planning. In suitable conditions (e.g., shallow cover), horizontal component data may also provide higher resolution images of the subsurface than traditional vertical component data (Garotta 2000; Krawczyk *et al.* 2012; Inazaki 2012; Polom *et al.* 2010; Pugin, Pullan, and Hunter 2010; Pugin *et al.* 2013; Bansal and Gaiser 2013; Malehmir *et al.* 2013b). This is particularly useful at shallow depths where a great need to link shallow and deeper structures is often desirable in order to take advantage of the detailed surface geological mapping/observations and available shallow boreholes.

In this study, we present a case study from a high-resolution three-component (3C) seismic landstreamer survey carried out in a mineral exploration site in Laisvall (Fig. 1), Northern Sweden. Technical reliability of the streamer has been thoroughly studied by Brodic, Malehmir, and Juhlin (2014) and by Brodic *et al.* (2015). The current landstreamer configuration, a prototype broadband (0–800 Hz) based on micro-electromechanical system (MEMs) sensors, consists of three segments with 20 3C sensors each 2 m apart and an additional segment with 20 3C sensors each 4 m apart, giving a total streamer length of 200 m. These segments can be towed in parallel or in series, which in combination with synchronized wireless and cabled sensors can address a variety of complex geological problems (Brodic *et al.* 2015). In this study, we used three segments with a total length of 160 m. The system is particularly geared for noisy environments and areas where high-resolution images of the subsurface are needed. It has little sensitivity to electrical noise and measures sensor tilt that can be compensated for during acquisition (if desired), potentially important in rough terrains.

Our targets in this study were: (i) structures down to and within the Precambrian crystalline basement; and (ii) a magnetic lineament (Fig. 2) crossed by the profile to test a hypothesis about the origin of the positive magnetic anomaly. It was speculated that the positive signature was due to either a basement high or a fault in the basement (e.g., Casanova 2010; Saintilan *et al.* 2015). In addition, we tested explosives and a 5 kg sledgehammer to generate the seismic signal. Therefore, a comparison between these two types of sources is also provided in this paper. We illustrate the potential of both 3C data and the landstreamer system for imaging structures possibly connected to mineralization, particularly at shallow depths where conductivity-based methods (e.g., electromagnetics) have difficulties due to the presence of strong conductors such as organic-rich black shale and graphite schist sitting above the basement and the mineralized units (Fig. 1b,c).

2 GEOLOGY OF THE STUDY AREA

Willdén (2004) provided an overview of the geology of the Laisvall area (Fig. 1), geological structures related to the mineralization, and potential scenarios explaining the ore genesis. The Laisvall mine is about 8 km north of the study area, and its geology is well documented (e.g., Christofferson *et al.* 1979; Rickard *et al.* 1979; Bjørlykke and Sangster 1981; Romer 1992; Lucks 2003; Casanova 2010; Saintilan *et al.* 2013, 2015) due to several decades of mining and exploration. We expect similar structures in our study area (Fig. 1c), apart from the absence of Caledonide nappes, which have been eroded away. The Laisvall deposit is a disseminated sandstone-hosted Pb-Zn-(Ag) one, located at the Caledonian front just south of the Arctic Circle in Northern Sweden (Fig. 1). It was mined for over half a century using underground mining methods, mainly room and pillar, by Boliden Mineral AB, until the mine was closed in 2001 due to a decline in the ore reserves (Willdén 2004). During the life of the mine, the Laisvall deposit yielded about 65 Mt of ore at 4.0% Pb, 0.6% Zn, and 9 g/t Ag (Willdén 2004).

The host rock of the mineralization is part of an extensive transgressive platformal sequence of sedimentary rocks, mainly sandstones and shales, developed on continent Baltica during Vendian–Ordovician times and now exposed along the c. 2000 km-long eastern border of the Caledonian mountain belt (Willdén 2004). This sequence was deposited unconformably on an eroded and leveled surface of Proterozoic and Archean basement rocks, belonging to the Fennoscandian Shield. The basement is primarily granitic to syenitic in composition (see Figs. 1 and 2; and see (Welin 1970)). The upper

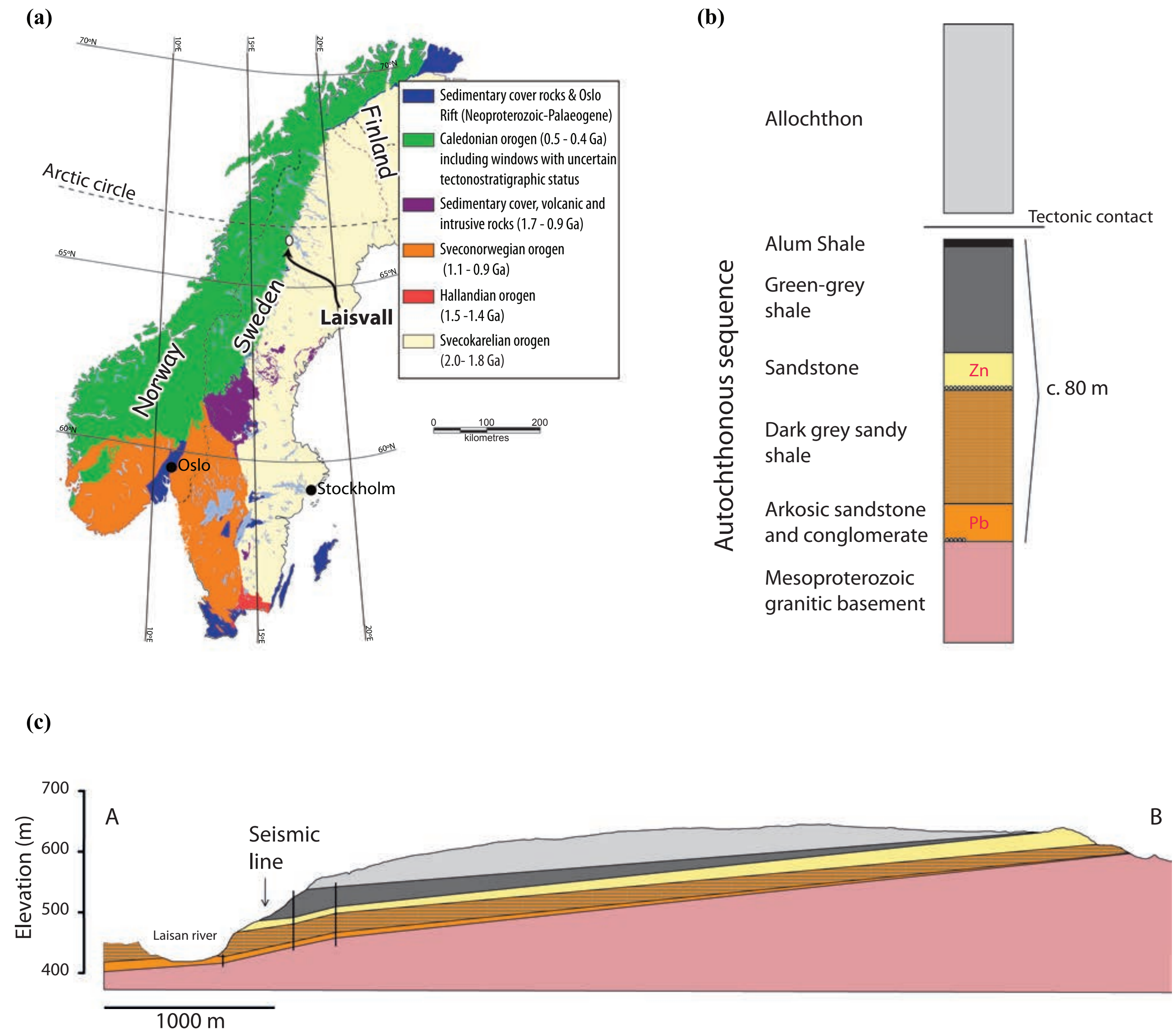

Figure 1 (a) Major tectonic units in Scandinavia (modified from (Gee *et al.* 2010)) with respect to our study area (Laisvall), located in the frontal part of the Caledonide Orogeny. (b) Simplified stratigraphic column in the study area (Boliden Mineral AB). (c) A schematic geologic cross-section (partly constrained by existing boreholes (thin vertical lines) and surface geological mapping) showing different stratigraphic units in the study area. See Figure 2a for the location of the cross section.

surface of the basement was a peneplain with isolated hills rising up to 50 m above the surroundings (Willdén 2004).

The transgression corresponds in time with the opening phase of the Iapetus Ocean and the establishment of a passive margin along the ancient continent Baltica (Gee 1975; Stephens and Gee 1985; Willdén 2004). The sedimentary cover, mainly shale and sandstone, i.e., the so-called autochthon (Fig. 1b, is overlain by various nappe complexes transported eastwards by thrusting during Silurian and Devonian times in connection with the Caledonian orogeny and final closure of the Iapetus ocean (Soper *et al.* 1992; Willdén 2004). The nappe complexes are present on the eastern and western sides of Lake Laisan but, due to erosion, are missing in our study area. The nappes are thought to have been emplaced after mineralization, and thus may only play a role in displacing the mineralization, as evidenced by over-thrusting of some of the deposits (Willdén 2004). The sedimentary rocks, the autochthon, are terminated upward by organic-rich black

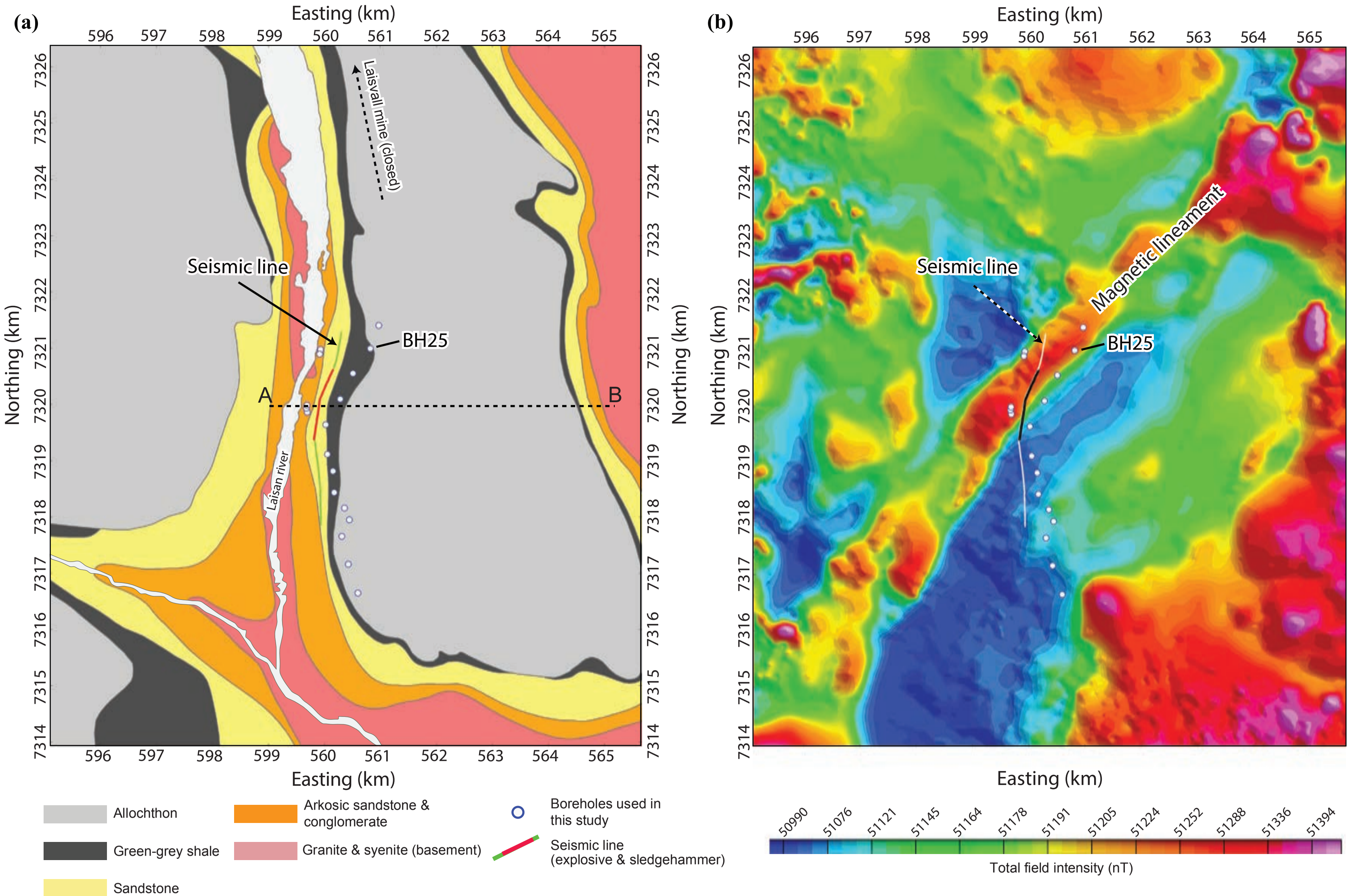

Figure 2 (a) Geological and (b) total-field aeromagnetic maps of the study area showing the location of the seismic line (explosive part in red and sledgehammer part in green) and existing boreholes. A geologic cross section along AB line is shown in Fig. 1c. Note that the seismic profile intersects a magnetic lineament, which was one of the targets of this study. Borehole 25 (labeled as BH25) intersects the magnetic lineament and is discussed later in the paper. Data kindly provided by the Geological Survey of Sweden. Geological map after Lilljequist (1973).

shale (Alum Shale Formation) that constitutes the principal sole of the thrust nappe sheets (décollement) and is often gently dipping (Hurich *et al.* 1989; Juhojuntti, Juhlin, and Dyrelius 2001; Gee *et al.* 2010; Hedin, Juhlin, and Gee 2012; Hedin *et al.* 2014). The shale formation is highly conductive (Rasmussen, Roberts, and Pedersen 1987; Korja *et al.* 2008) and often the main conductor in electromagnetic surveys in the Swedish Caledonides (Boliden Mineral AB, *personal communication 2013*). Its high conductivity, associated with its occurrence close to the surface, prevents accurate delineation of sub-shale structures using electromagnetic methods, including basement highs and lows and any mineralization associated with them within the sandstone. The study area is located stratigraphically below the Alum Shale (Fig. 1).

While there are numerous magnetic lineaments observed on the magnetic map of the study area and its surrounding areas (e.g., Fig. 2b, their origin and relationships with the mineralization has been a matter of debate (Christofferson *et al.* 1979; Rickard *et al.* 1979; Bjørlykke and Sangster 1981; Romer 1992; Lucks 2003; Casanova 2010; Saintilan *et al.* 2013, 2015). Two scenarios have been discussed: (i) mafic-dykes in the basement, or (ii) faulting/brittle structures in the basement, the latter being important since it may imply local hydrothermal fluid circulation to form some of the deposits (Saintilan *et al.* 2015). In the study area, there is no evidence from boreholes suggesting the presence of mafic dykes or intrusions in the basement. A fault in the study area with a positive magnetic signature is of great interest since it may reflect mineralization within and adjacent to it. Two ore genetic models have been proposed for the sandstone-hosted Pb-Zn deposits of the Laisvall area on the basis of the metal-bearing solution (Bjørlykke and Sangster 1981), a hydrothermal or basin-brine model, and/or ground water or meteoric model (Willdén 2004).

The study area hosts a number of small deposits in both the autochthonous and allochthonous rocks. During 1940–1960, a series of boreholes were drilled, providing detailed information about the geology. The stratigraphy in the area can be summarized as follows (Fig. 1):

- A basement with a granitic to syenitic composition;
- Overlying the basement is a c. 10 m-thick coarse-grained arkosic sandstone. A conglomerate is sometimes found at the basement contact. This sandstone is occasionally richly mineralized with Pb and CaF_2;
- The sandstone is overlain by a c. 30 m-thick organic-rich shale/schist that is interlaminated with thin beds of sandstone;
- A c. 10 m-thick coarse-grained sandstone follows the sequence with a thin conglomerate in the bottom. The sandstone can be divided into two distinct units (lower and upper), where the lower unit is more clay rich. The upper sandstone is weakly Zn-mineralized over a wide area;
- A more than 30 m-thick package of shale/schist follows the sequence with a thin graphitic shale on the top, which correlates with the Alum Shale.

The seismic survey (Figs. 1 and 2) was carried out along a profile that cuts the stratigraphy at different levels. The Pb-rich mineralization encountered in the lowermost coarse-grained sandstone appears to coincide with a linear aeromagnetic anomaly and was the reason this site was chosen for the seismic study.

3 PETROPHYSICAL MEASUREMENTS

Petrophysical measurements on a few core samples were carried out at the scale of a few centimetres in order to provide some complementary information about potential structures resolved in the seismic and radio-magnetotelluric (RMT) data. Table 1 summarizes the main results. From these measurements and a rough estimation of impedance contrasts, we conclude that the basement rocks have potential to be reflective and magnetic. An interesting observation is that graphitic schists show a higher density compared with other rocks (except the mineralized sandstone), implying they can also be reflective if juxtaposed with, for example, sandstone. Velocity measurements were conducted on samples using a 1 MHz frequency transducer; thus, the values cannot be directly compared with those measured in the seismic frequency range. Nevertheless, a velocity contrast at even lower (or seismic) frequency ranges may be possible for crystalline rocks given their low porosity (e.g., Malehmir *et al.* 2013b). The measurements suggest that the potential to generate converted waves is likely given the thin layering of the strata and strong velocity contrasts. Graphitic schists, although not measured in this study, are expected to be strongly conductive in the study area.

4 SEISMIC SURVEY

4.1 Data acquisition

To generate the seismic signal, 20 g–40 g of dynamite fired at a depth of about 0.7 m–1.5 m was used in the area where the magnetic lineament is observed (Fig. 2b). We chose dynamite in this part to increase the potential to image successfully the

Table 1 Average physical properties measured on a few core samples obtained from the study area suggesting that basement (syenitic and if faulted) and sandy schist rocks as well as mineralized sandstone can be reflective, graphite-rich schist can also be strongly conductive (not measured here) and gneiss, and the mineralized sandstone can be strongly magnetic. The measurements suggest that the potential to generate converted waves is likely given the thin layering of the strata (Fig. 1) and strong velocity contrast observed here.

Lithology	Density (gr/cm^3)	P-wave velocity (km/s)	S-wave velocity (km/s)	Magnetic susceptibility ($\times 10^{-3}$ SI)	No. of samples
Basement (syenite)	2.61–2.68	3.3–5.6	2.1–3.2	0.1–1.3 (often low)	3
Basement (gneiss)	2.67–2.68	5.2–5.5	3.2	0.18–1.2	2
Arkosic sandstone	2.61–2.64	4.3–5.2	NaN	Very low	2
Schist-graphitic	2.79 2.79	4.3–4.4	NaN	0.5–0.6	2
Coarse-grained sandstone	2.65–2.7	4.2–4.9	2.5	Very low	4
Mineralized sandstone (minor ZnS-PbS)	3.0	5.6	3.6	1.32	1

top of the basement using refracted arrivals. Inspection of the quality of the first arrivals during the data acquisition, particularly at far offsets, confirmed that dynamite was more suitable for this target compared with the sledgehammer. Clear first arrivals at a given offset suggest signal penetration to a depth corresponding to at least the given offset. A shot spacing of 10 m was used, and eight shots were fired before the streamer was moved to a new position (80 m forward). Shots were only fired within the 2 m-spaced sensors, i.e., the 80 m tail was (three 3C-MEMs-based segments were used in this study) overlapped with the previous streamer position. A total of 130 shots were fired using explosives, the streamer was moved 17 times, and about 1.3 km of the profile was covered within 2.5 days.

The remaining part of the profile, i.e., the southern and northern ends (in green in Fig. 2a, was acquired using a 5 kg sledgehammer with three hits at every shot location. A source spacing of 2 m–4 m was used, and about 20 source locations were recorded before the streamer was moved to a new position (80 m forward). Again, sources were only activated within the 2 m-spaced sensors so that there was overlap along the 80 m tail. More than 650 sledgehammer source locations were activated, the streamer was moved 33 times, and about 2.4 km of the profile was covered within 2.5 days. A total of four persons took part in the data acquisition, and an average of 500–800 m/day of seismic data were acquired.

Figure 3 shows a photo taken from the seismic landstreamer during the data acquisition in the study area. The third segment of the streamer is shown here; in this segment, sensors are spaced at every 2 m. The whole streamer was towed using a four-wheel drive vehicle (Fig. 3) where a seismic observer was responsible to carry out the data recording, quality control, and driving of the vehicle. Prior to the seismic acquisition, about 40 cm of fresh snow had to be plowed by the crew. The acquisition vehicle towed a large tyre for this purpose. Temperature varied from +2°C during the days to −20°C in the late afternoon and overnight. Overall this allowed good coupling between the streamer and the surface and, thus, contributed to good quality seismic data. We moved the streamer forward at the end of each day but recorded along it the following morning. This enhanced the ground coupling due to the freezing conditions overnight. A summary of the main acquisition parameters is shown in Table 2.

Generally, the seismic data show good quality, likely due to the good coupling between the sleds and the frozen and snowy ground. To provide some information about the reliability of the streamer for this study, we present an example of an explosive shot gather and particle motion plots (hodograms) for some noticeable features in the 3C data (Fig. 4). Clear first P-wave and S-wave arrivals, as well as surface waves, are observed in the 3C data. For example, the hodograms show that the P-wave arrivals (first break time window) are dominant in the vertical component data (e.g., Fig. 4d, e). Noise appears (gained 100–300 times) to be not predominantly random, but some energy is coming from the side (stronger on the crossline data). We speculate this to be from the river (and wind) just a couple of hundreds of metres away from the line (Fig. 2a). Nevertheless, the noise looks very weak to have any significant effect on other wave types. Shear and surface waves show their own clear patterns with respect to vertical and horizontal motions (e.g., elliptical for the surface wave).

Figure 5 shows an example shot record from the explosive data for all the three components. First arrivals are clearly observed in the vertical component data. Clear

Figure 3 Photo showing the 3C seismic landstreamer system of Uppsala University used for the data acquisition in this study. Only the third segment of the streamer is seen in this photo. Three segments with a total length of about 160 m were used in this study. Note snow and frozen ground conditions during the data acquisition.

Table 2 Main 3C reflection seismic and RMT data acquisition parameters, November 2013.

	Explosive	Sledgehammer	RMT
Survey parameters			
Recording system	SERCEL 428	SERCEL 428	EnviroMT
No. of receivers	60	60	——
No. of shots	130	650	Up to 18 transmitters
Receiver interval	2–4 m	2–4 m	10 m
Shot interval	10 m	4 m	——
Maximum source-receiver offset	160 m	160 m	——
Source size	10–40 g dynamite	5 kg hammer	Passive (14–250 kHz)
CDP size	2 m	2 m	——
Profile length	1300 m	2400 m	900 m
Spread parameters			
Record length	10 s (1 s used)	10 s (1 s used)	50 times power stacking
Sampling rate	1 ms	1 ms	2 MHz
Receiver and source parameters			
Sensor	3C-MEMs	3C-MEMs	Electric and magnetic fields
No. of sensors	Single	Single	Two horizontal electric & two horizontal and one vertical magnetic
Source pattern	Single/point	3 impacts/point	Vertical electrical dipoles
Source depth	0.7–1.5 m	0 m	——

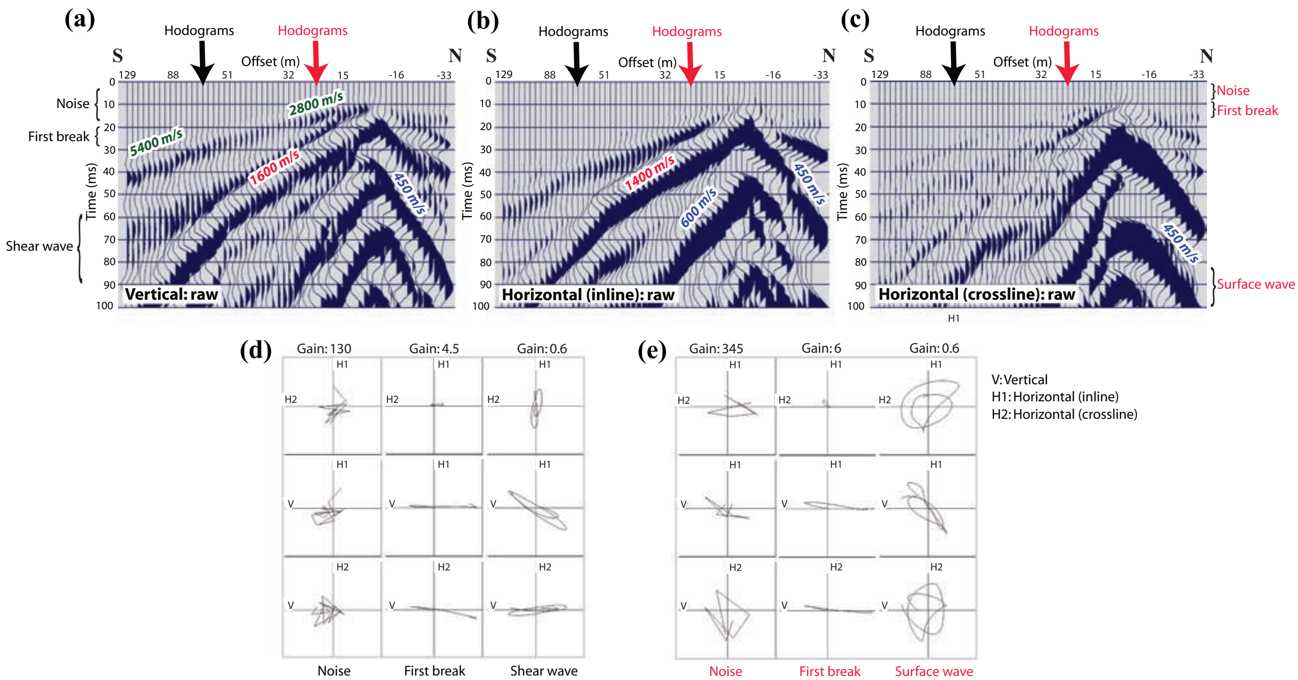

Figure 4 Example explosive shot gather recorded by the streamer and shown for (a) vertical (b) horizontal inline and (c) horizontal crossline data. Hodograms of some of the main waves in the shot recorded at two different receiver locations are presented in (d) and (f). The hodograms illustrate the reliability of the streamer in registering particle motions as they are expected to be. Also note that the sensor arrow (North arrow) is pointing towards the source for the hodograms shown here. For display purposes, the seismic data had to be gained differently.

direct and refracted arrivals (e.g., Fig. 5a) were crucial in obtaining a good static solution and high-resolution images of the subsurface structures. The absence of direct and refracted P-wave arrivals in the horizontal component data is a good indication that the P-wave incidence angle is close to vertical and do not strongly contaminates the horizontal components (e.g., Fig. 5d, g). The raw explosive data have useful bandwidth up to 400 Hz signal that appears only limited by the anti-alias filter for 1 ms sampling interval (Table 2).

The strong wind on most days, with occasional snow (and even some rain), had some influence on the quality of the horizontal component data. Figure 6a shows a sledgehammer source record for all the three components (mixed traces; every third trace is vertical component). Far offset traces are strongly contaminated by coherent noise (red arrow in Fig. 6a). The three repeated hits at every source location, and their vertical stacking, helped to significantly reduce the noise, particularly at far offsets (Fig. 6b). Figure 6c–e, respectively, show the vertical, horizontal inline, and horizontal crossline components of the source record. A wide-angle reflection is noticeable in the vertical component data (red arrow in Fig. 6c), whereas the horizontal components (Fig. 6d,e) do not appear to contain useful information. Interestingly, a careful analysis of the amplitude spectra of the source gathers of the three components suggests that the high-frequency content of the sledgehammer data is primarily dominated by noise (wind noise) since it is dominantly observed in the horizontal component data and not in the vertical component. This is fairly obvious when the actual records of the three components are compared against each other (e.g., red arrow in Fig. 6e).

4.2 Data processing

Table 3 summarizes the main processing steps applied to the data. In this paper, we only use the common midpoint approach for processing the data given the shallow depth of the targets and the relatively short offsets (i.e., no mode-converted processing using asymptotic binning (Thomsen 1999; Stewart *et al.* 2002), e.g., P-S or S-P was attempted; this will be the focus of future studies). Moreover, only 3C processing results from the explosive data are presented here since the sledgehammer data did not contain useful shear-wave signal; it appears relatively weak compared with the explosive data (c.f., Figs. 4 and 6). Therefore, we only present P-wave

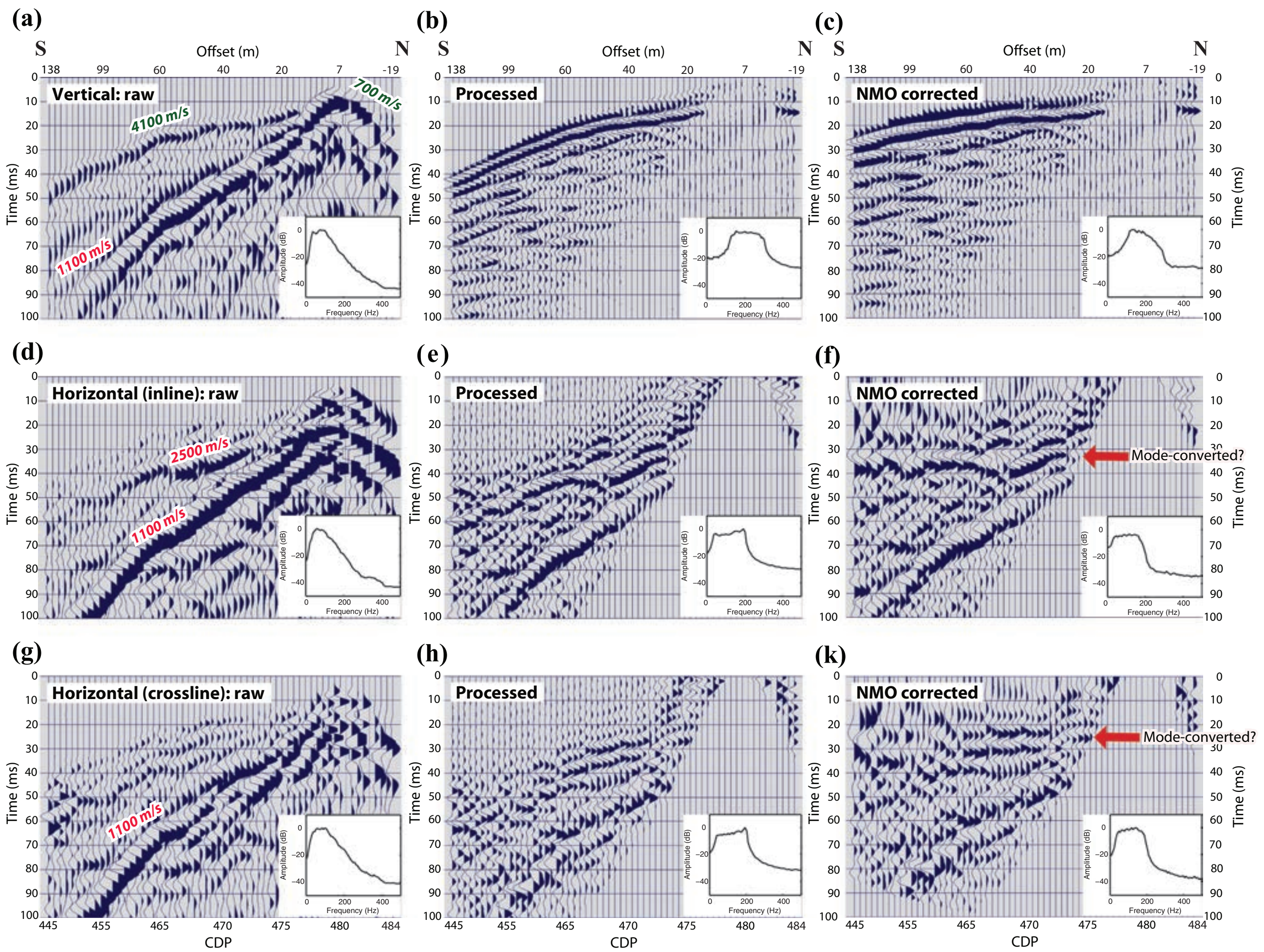

Figure 5 Example of raw source gather and its amplitude spectrum (0–100 ms data window) from the explosive data shown for all three components (a) vertical, (d) horizontal inline and (g) horizontal crossline components; (b, e, and h) are the processed (after band-pass filtering, refraction static corrections, FK filtering and surgical mute) versions of (a, d, and g), respectively; (c, f, and k) are the NMO corrected (using 4200 m/s for vertical component and about 2700 m/s for horizontal inline and 2200 m/s for horizontal crossline components) versions of (b, e, and h), respectively. Note the reflection marked by the red arrows (labeled as "Mode-converted?") at about 20 ms–30 ms on the horizontal component data (f and k). Various features, for example the direct arrivals with 700 m/s velocity (a), and their apparent velocities are also labeled.

processing results (vertical component data) from the sledgehammer data. Source–receiver azimuths were corrected for the two horizontal components, although the effect was minimal given that the shots were fired next to the seismic line. The key processing steps were: (i) refraction static corrections; (ii) noise attenuation; (iii) velocity analysis, and (iv) poststack coherency enhancements.

Given the high quality of the first arrivals in the vertical component data (e.g., Fig. 5), a good P-wave refraction static solution was obtained with a misfit of about 1 ms for the first arrivals that were first picked automatically and then manually inspected and corrected where needed. For the horizontal component data, we were unable to pick any obvious and consistent direct and refracted shear-wave arrivals. Thus, the P-wave statics obtained from the vertical component data were doubled and used for the horizontal component data. We also made an attempt to use the P-wave static model and replace the velocity of the overburden and the bedrock with what we thought would be reasonable in this environment, but this did not provide convincing results. High-frequency noise and strong coherent noise, attributed to the wind (and occasionally rain), were attenuated by filtering frequencies above 220 Hz. Ground roll was partly attenuated by filtering frequencies below 70 Hz, and the remaining parts were

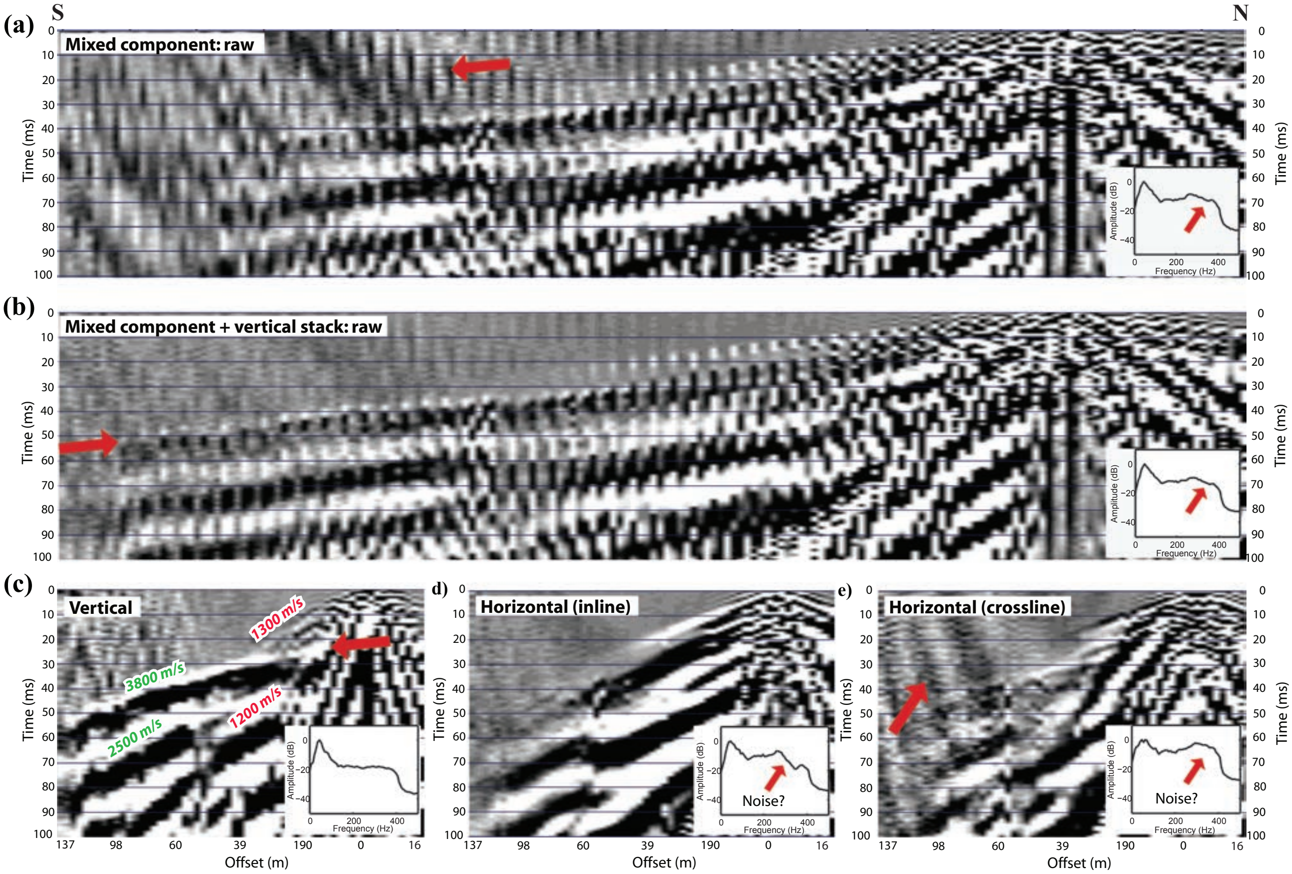

Figure 6 An example raw shot gather from the sledgehammer data and its amplitude spectrum (whole data window; 0 ms–100 ms) shown for the mixed three components (every third trace is vertical component), (a) only one impact, (b) vertical stacking of three impacts, (c) separated vertical component, (d) separated horizontal inline component and (e) separated horizontal crossline component. Note improvements in the signal-to-noise ratio after the vertical stacking of the three impacts and the reflection observed in the vertical component data (c). The high-frequency parts of the amplitude spectra appear to be from noise. This is more evident in the horizontal component data than in the vertical component data.

attenuated using an FK filter designed to attenuate steeply dipping events in the shot gathers. First, we applied a normal moveout (NMO) correction using a velocity of about 4200 m/s to the shot gathers and then applied the FK filter. The NMO correction was then removed after the FK filtering. This significantly helped to clean the shot gathers from the ground roll, as shown in Fig. 5b, and revealed some wide-angle reflections. A similar approach was implemented on the horizontal component data. Finally, a surgical mute was applied to remove the remaining surface waves, which were significantly stronger on the horizontal component data, particularly the inline component (Fig. 5e,f).

Careful inspection of the processed shot gathers suggests the presence of wide-angle reflections in the vertical component data and a shallow reflection (about 20 ms) in the horizontal crossline component data. Figure 5f,k illustrates the value that horizontal component data can offer. For example, the reflection observed in the processed horizontal crossline component data (e.g., red arrow in Fig. 5k) is not at all observed in the vertical component data. At about 20 ms, only first arrivals are observed on the vertical component data. The shot gathers (Fig. 5c,f,k) are shown after an NMO correction of 4200, 2700, and 2200 m/s, respectively. Given these NMO velocities for the horizontal component data and that the reflections arrive before the first direct shear-wave arrivals, we interpret these reflections to be mode-converted (i.e., P-S) reflections (e.g., Fig. 3f,k; although somewhat different in character in the inline and crossline components). A rough NMO correction velocity for a mode-converted reflection is the square root of the product of the P- and S-wave velocities (e.g., Tessmer and Behle 1988), and this is consistent if we assume a velocity on the order of 4500 m/s for the P-waves

Table 3 Principal seismic data processing steps applied to all the three component data. Note that no converted-mode processing was attempted in this study and only pure vertical- and shear-wave data processing was carried out. Horizontal component data from sledgehammer records did not contain useful shear-wave signals thus they are not presented and nor discussed in this study.

Step	Parameters
1.	Read 10 s SEGD-- data (only 1 s used)
2.	Construct and apply geometry (CDP bin size 2 m)
3.	Phase rotation (only horizontal components, source-receiver azimuths)
4.	Trace editing
5.	Pick first breaks: only vertical component, full offset range, automatic neural network algorithm but manually inspected and corrected
6.	Refraction static corrections vertical: datum 495 m, replacement 3500 m/s, v_0 600 m/s horizontal: datum 495 m, twice the vertical component
7.	Geometric-spreading compensation: v^2t
8.	Band-pass filtering explosive-vertical: 50–70–220–260 Hz; horizontal: 30–50–220–260 Hz sledgehammer-vertical: 30−40−180−210 Hz
9.	Spectral whitening explosive-vertical: 30–50–200–220 Hz; horizontal: 40–50–200–220 Hz sledgehammer-vertical: 40–50–160–180 Hz
10.	Direct shear-wave muting (near-offset) or attenuation (far-offset)
11.	Air-blast attenuation
12.	Trace balance using data window
13.	Velocity analysis: iterative
14.	Residual static corrections: iterative
15.	FK-filtering targeting steep events
16.	Normal moveout corrections (NMO): 70% stretch mute
17.	Stack
18.	f_x-deconvolution
19.	Band-pass filtering explosive-vertical: 30–40–160–180 Hz; horizontal: 20–30–130–150 Hz sledgehammer-vertical: 30–40–160–180 Hz
20.	f_x-deconvolution
21.	Trace balance: 0−200 ms
22.	Migration: finite-difference (only vertical component)
23.	Time-to-depth conversion: constant velocity vertical: 4200 m/s horizontal: 2300–2500 m/s

and 1500 m/s for the S-waves. The assumed S-wave velocity is very slow but consistent with observed direct/refracted shear wave arrivals. We later refer to this reflection in our final seismic image to argue that it is real and not an artifact of our processing approach.

Two rounds of velocity analyses combined with surface-consistent residual static corrections helped to image a strong reflection at about 20 ms–30 ms in the unmigrated seismic sections. Note that the horizontal inline data required higher velocities (about 2700 m/s) to constructively stack than the crossline data (about 2200 m/s). This may imply that, in the direction of the seismic profile (inline), structures may have faster shear-wave velocity than perpendicular to it (indirect evidence for anisotropy). Further work is required to fully explore and exploit the anisotropy signatures in the data. Poststack processing steps mainly involved FX-deconvolution and trace balancing, as well as migration and time-to-depth conversion. We preferred to not migrate the horizontal component data since the main reflections are horizontal, and the dipping ones were not fully preserved after an attempt of migration. We take this into account when interpreting the results (e.g., the actual dip is greater than the apparent dip).

5 RADIO-MAGNETOTELLURIC SURVEY

The RMT method is a passive-source electromagnetic method where the signal sources are distant radio transmitters operating in the frequency range from 14 kHz to 250 kHz. At such distances, the electromagnetic signals are considered plane waves and can be used to estimate the electrical resistivity of the near-surface structures (Bastani 2001; Bastani *et al.* 2009; Shan *et al.* 2014). RMT data are generally comprised of the three components of the magnetic field and the two horizontal components of the electric field. In the frequency domain, the electric and magnetic field components are related through the impedance tensor. Pedersen and Engels (2005) showed that 2D inversion of the determinant data is more robust than transverse-magnetic and transverse-electric mode inversions in a 3D environment. Following their recommendation, we carried out the 2D inversion using the determinant data.

5.1 Data acquisition

RMT data were measured at every 10 m along a portion of the seismic profile, mainly along the section where explosives were used (Fig. 2). During the acquisition period, the number of available transmitters was relatively stable. On average, about 20 transmitters could be detected, although this number decreased to about 15 or less in the afternoon. The operating frequencies of these transmitters ranged from 14 kHz to 250 kHz during the measurements. The frozen and snowy ground was not optimal for RMT measurements. The snow and ice had to be removed in order to plant the electrodes in the ground. In spite of the conditions, the RMT data generally show good quality, although they are occasionally noisy. Noisy data were removed and replaced by linear averaged values at the adjacent stations that had better quality data. The raw apparent resistivity and phase data are shown in Figure 7.

5.2 Inversion

We used EMILIA software (Kalscheuer *et al.* 2013) to run 2D inversions of the RMT data. An error floor of 0.09 and 0.045 was used for apparent resistivity and phase, respectively. A damped Occam regularization type (Kalscheuer *et al.* 2013) with a horizontal to vertical smoothing of three was used. Up to ten iterations were required to obtain a misfit of 4.3%. This high RMS misfit is probably due to the frozen ground, which introduced a higher contact resistivity than normal. We did not push the inversion too far and accepted these results.

6 RESULTS

Given the high quality of the first arrivals on the vertical component data, particularly for the explosive source gathers (Figs. 4 and 5), and to complement the processing results, we also performed tomographic inversion of the first arrival travel times using an inversion code provided by Tryggvason, Rögnvaldsson, and Flovenz (2002) (also see Podvin and Lecomte 1991; and Hole 1992). We obtained an RMS value slightly more than 1 ms. Figure 8 shows the travel-time residuals computed for all the offsets obtained in the final iteration (nine iterations were run).

Figure 9a shows the final RMT model that essentially shows a resistive layer underlying a more conductive cover. To check the depth penetration of the RMT data, we used the method (C(omega)) introduced by Schmusker (1970) and Spies (1989). This showed that the conductive layer is partly resolved by the RMT data (see the dots in Fig. 9a). Further synthetic tests, not presented here, were also performed and showed that resolving the conductive layer using the RMT frequencies available at the site is highly possible.

The tomography results are shown in Figure 9b. Seismic processing of the explosive source data for the vertical, horizontal inline, and horizontal crossline components are shown in Figure 9c–e, respectively. Sledgehammer data, only vertical component, are shown in Figure 10. The horizontal component data, particularly the horizontal inline component (Fig. 9d), are clearly much noisier than the vertical component data, but they do show some reflections. We now discuss the results on the basis of the different seismic sources.

6.1 Explosive data

The vertical component data show a strong reflection at a depth of about 50–60 m and indicate an undulated surface where the magnetic lineament is observed (Fig. 9c). The reflection is shallowest at common depth point (CDP) of about 200 where a small water stream crosses the profile. The good quality of P-wave first arrivals allows us to be confident of our refraction statics model, which is also shown on the seismic sections (purple lines) for all three components. A comparison between the depth to the first refractor (interpreted to be the overburden-bedrock contact and estimated from the refraction static solution) and the reflections guarantees that

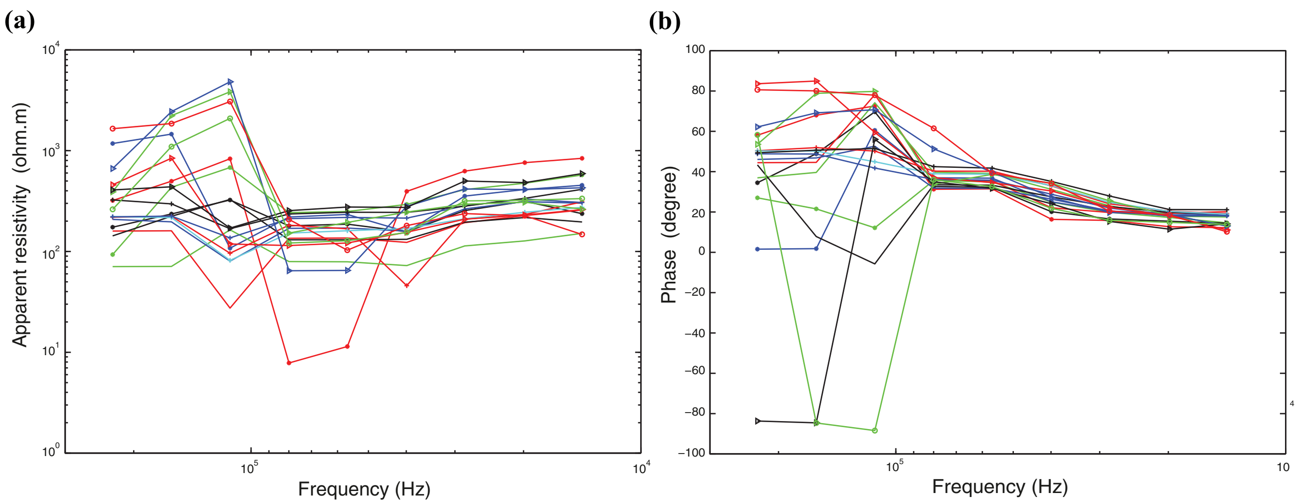

Figure 7 Raw RMT data, after the removal of noisy data, showing (a) apparent resistivity and (b) phase. Only one sounding curve is shown for every 5th station. In total, 94 stations that are 10 m apart were measured during three days. Note that the apparent resistivity data have a better quality in contrast to the phase data.

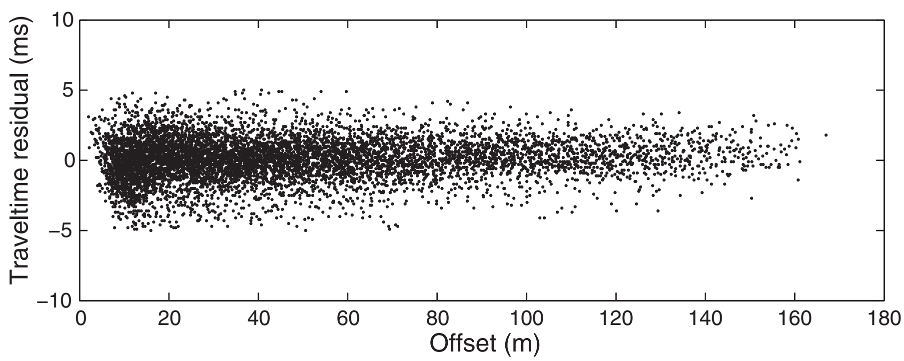

Figure 8 Traveltime residuals (observed minus forward calculated) computed for all the offsets from the last tomographic inversion. An RMS value slightly above 1 ms was obtained.

we are not imaging the overburden-bedrock contact in these sections but more likely the lithological contacts. We interpret the strong reflection in the vertical component data as originating from the top of the crystalline basement. This implies that no lithological contact above the basement is clearly imaged in the vertical component data. The high-velocity structures of the tomographic model are not likely reflecting the basement structure above it. They more likely indicate high-velocity structures close to the surface, but neither outcrop data nor available borehole data support this.

Horizontal crossline component data show a strong sub-horizontal reflection at about 30 m depth (Fig. 9e), depending on the velocity used for the time-to-depth conversion, where the unconstrained RMT inversion model also shows a resistivity contrast around this depth (Fig. 9a). This reflection is clearly observed in several processed shot gathers such as the one shown in Figure 5k. In particular, a steeply dipping reflection at the location of the positive magnetic lineament is clearly observed in the horizontal crossline component data but not in the vertical component data. The vertical component data, however, better image the top of the crystalline basement and, together with the horizontal crossline component data, suggest that the steeply dipping reflection extends into the basement and crosscuts the shallower stratigraphy. The horizontal inline component data show a similar sub-horizontal reflection as the horizontal crossline component data, but at a depth of about 50 m and with a rather different character than the two other components. It is not clear what generates this reflection. Note that this reflection required slightly higher NMO velocity (see section 4.2) to be imaged than the reflection in the horizontal crossline component data.

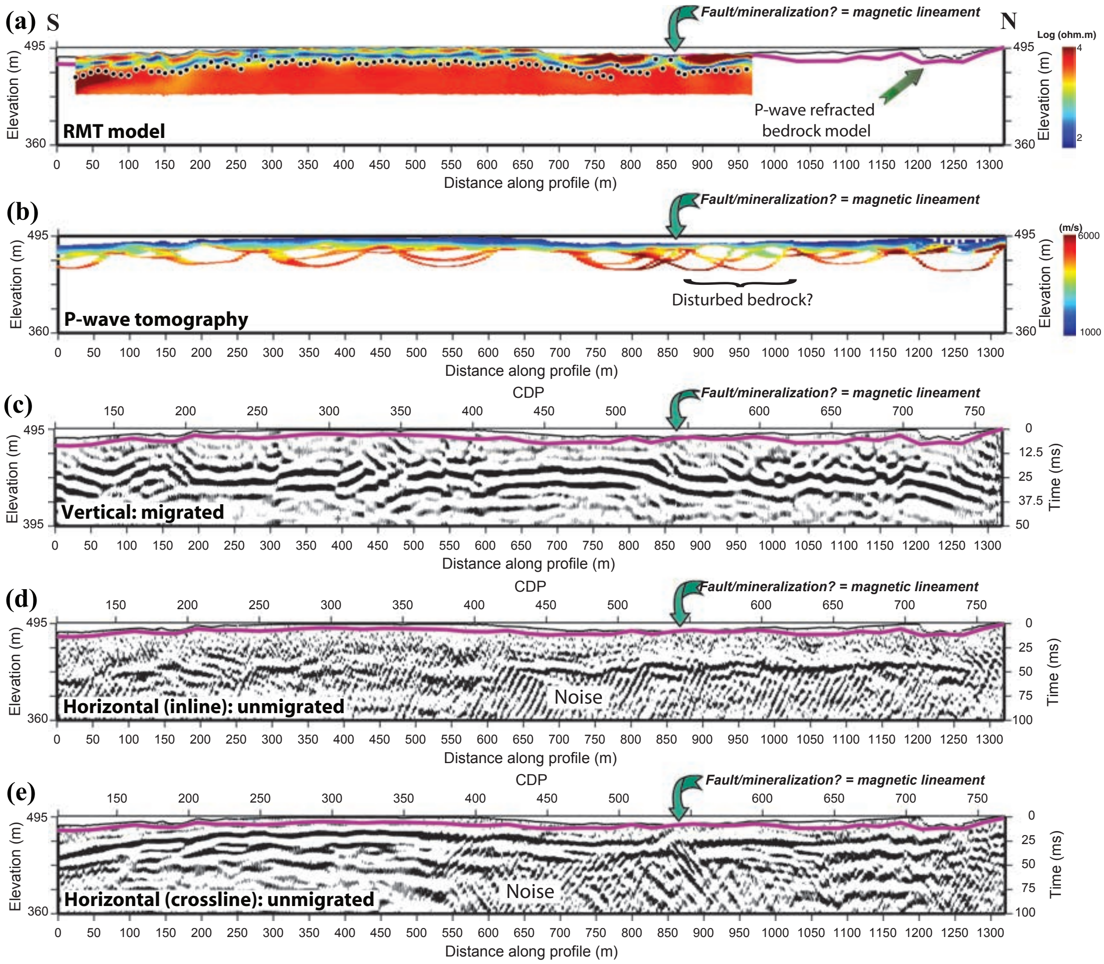

Figure 9 (a) RMT model along a portion of the explosive line (dots show the estimated penetration depth of the data), (b) P-wave first arrival tomographic results, (c) migrated and time-to-depth converted vertical component seismic section, (d) unmigrated, but time-to-depth converted radial component (horizontal inline) seismic section, and (e) unmigrated, but time-to-depth converted transverse component (horizontal crossline) seismic section. Purple line is the P-wave refraction static model for the first refractor. Seismic sections shown here are from the explosive data. The location of the magnetic lineament is also shown using an arrow. This location appears to be associated with a major fault system and a steeply north dipping reflection in the horizontal crossline component data.

A close-up image of the vertical and horizontal crossline component data in the area where the magnetic anomaly is observed is shown in Figure 11. We show unmigrated results here for a direct comparison between the two components. Figure 11a shows again the horizontal crossline component results but this time superimposed on the RMT results (Fig. 9a). A good correspondence between the two results is observed. A comparison between the two unmigrated seismic sections suggests the occurrence of two major faults and a depression (a low-level topography) in the basement at a distance of about 880 m to 950 m along the explosive line in the vertical component data (Fig. 11b). No basement reflector is imaged in the horizontal crossline component data, but instead, a shallower sub-horizontal reflection is interpreted to be from the contact between graphitic schist (conductive) and sandstone (resistive) (see also Fig. 11a). If our interpretation of the two faults in the vertical component data is correct, then the horizontal crossline component data have successfully imaged one major fault plane (or zone) associated with one of them and several smaller ones within the sandstone (smaller white arrows in Fig. 11c). In summary, the explosive data in conjunction with the RMT data have allowed the delineation of three major contact boundaries, namely the overburden-bedrock contact (sandstone-to-graphitic schist), schist sandstone, and sandstone-crystalline basement and a major fault system.

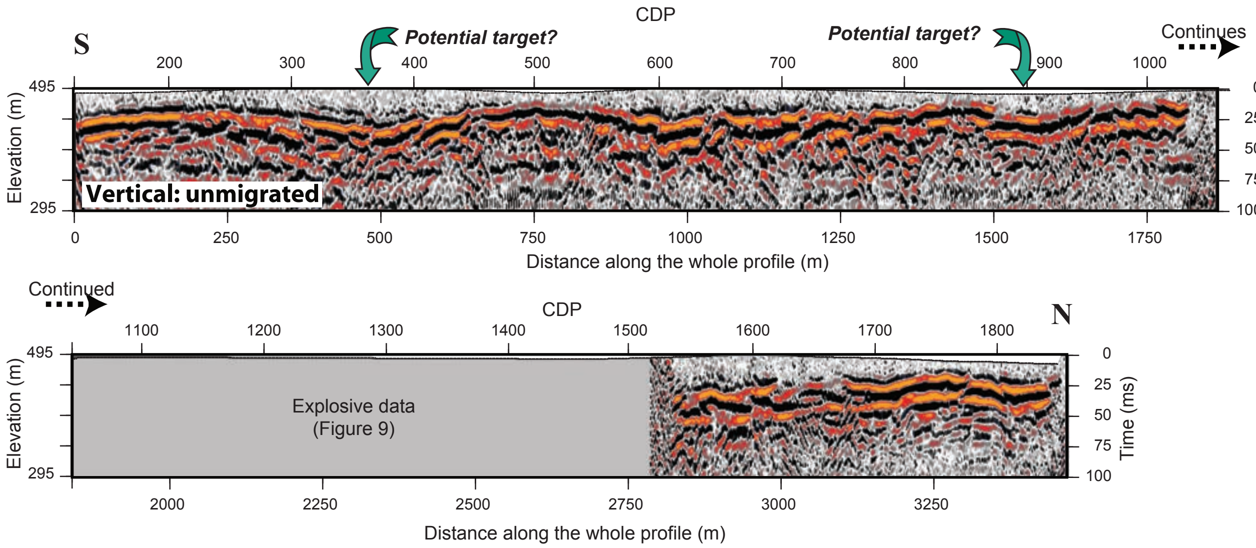

Figure 10 Unmigrated, but time-to-depth converted vertical component seismic section of the sledgehammer data. Explosive data are shown in Figure 9 and have a different CDP numbering. Two major basement depressions (maximum depth around 80 m–90 m) in the southern parts of the line are interesting targets for mineral exploration. Sledgehammer data did not contain sufficient shear-wave signal; therefore, only vertical component data are presented. The seismic section is shown into two panels for display purposes.

6.2 Sledgehammer data

Processing results of the sledgehammer data also suggest a strong reflection in the vertical component data (Fig. 10). This reflection is clear in most processed source gathers and, thus, is real and not an artifact of the processing. We again interpret this reflection as originating from the basement with its deepest (about 90 m) and shallowest (about 30 m) points at distances of about 500 m and 3300 m along the seismic profile, respectively (Fig. 10). Depressions in the basement such as the one reaching to a depth of about 90 m can be potential targets for mineral exploration. The sledgehammer data allow mapping of the crystalline basement surface to depths of at least 90 m in this type of environment. There is a shallower basement depression at a distance of about 1600 m along the seismic profile (Fig. 10), which could also be a potential target for mineral exploration in the study area.

7 DISCUSSION

In order to verify the steeply dipping reflection observed in the horizontal crossline component data (Figs. 9e and 11c), we carefully inspected the shot gathers in the area where it was observed. Figure 12 shows an example shot gather around that location. For comparison, CDP numbers corresponding to each trace are also provided. Note that the processed shot gather of all the three components shows some evidence of this reflection (or structure). The vertical component data (Fig. 12a,b) show a reflection merging with the first arrivals but too close to them (see red arrow in Fig. 12b) to be preserved in the data processing. The first arrivals (red arrow in Fig. 12a) also show a low velocity zone at about 65 m offset. A careful inspection of the first arrival times suggests that the low-velocity zone, if dipping, should be dipping towards the shorter offsets, or towards the north, consistent with the reflection image (Fig. 11c). The frequency content of the first arrivals also changes rapidly at this location; it is higher in the southern than the northern parts. This is consistent with our observation of the steeply dipping reflection in the horizontal component data. Both horizontal inline and crossline components show a short reflection in their processed shot gathers at the same location and clearly suggest a dip towards the north (Figs. 9e and 12d). The reflection extends to the direct (or refracted) P-wave and ends at where S-wave arrivals are interpreted to be present (i.e., likely a P-to-S steeply dipping mode-converted reflection).

Figure 13a,b shows close-up images of the P-wave first arrival tomographic results superimposed on a portion of the unmigrated vertical and horizontal crossline components, respectively. Although it appears to be difficult to provide a direct comparison between them, a disturbed velocity zone and perhaps some indications of faulting could be argued in the vicinity of where the magnetic lineament is observed. On the northern side of the interpreted fault, structures

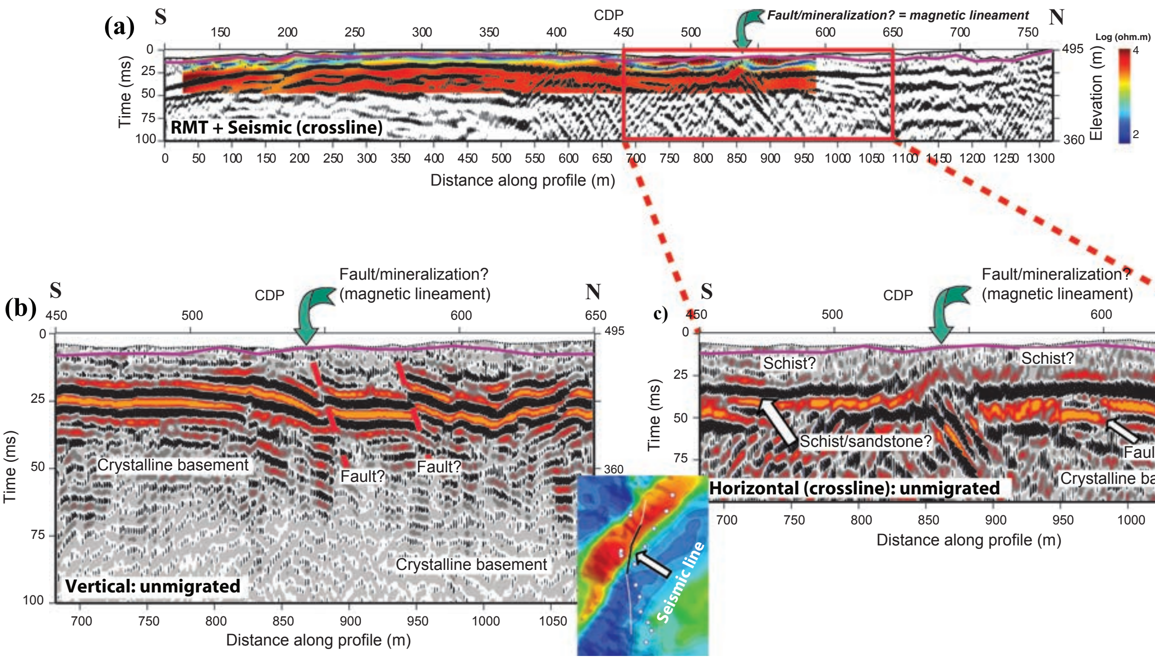

Figure 11 (a) Unmigrated, but time-to-depth converted, section of the transverse component data superimposed on the RMT results showing an excellent correspondence between the two data sets (see Fig. 9a, e). A portion of (b) unmigrated vertical and (c) transverse-component data suggesting two major fault systems in the vertical component data, and a major fault plane and smaller faults in the transverse component data. The magnetic lineament (Fig. 2) is likely associated with these structures. Note that the sub-horizontal reflections in these sections have two different origins and are from two different depths, one likely from the crystalline basement (50 m–60 m depth) and another from the contact between schist and sandstone (25 m–30 m depth), respectively. Again, the purple line on the sections shows the estimated depth to the bedrock using first arrivals of the vertical component data.

have much lower velocities and are more discontinuous. These analyses of the data further illustrate the potential of 3C data, particularly for shallow subsurface imaging and interpretation.

We interpret the reflections imaged in the horizontal component data as mode-converted waves and preserved in the final images, although no dedicated mode-converted processing approach was used to process these data. Hodograms of these reflections did not provide strong evidence about their origin. Some hodograms indicated shear-wave splitting signature, but this was not consistent through all the traces. The fact that these reflections occur mainly on the near offsets (e.g., Fig. 5f, k) or have a very steeply dipping character indicate they originate within the plane of the profile. A careful inspection of the steeply dipping reflection observed in the shot gather shown in Figure 12d,f suggests that it arrives earlier (about one wavelength) in the crossline component data than the inline component data. This favors the orientation of the reflector with regard to the orientation of the seismic line. While this is speculative in the absence of other convincing evidences (such as hodograms), we think that if any structure cuts the seismic profile at a right angle (Fig. 2b), one could expect faster shear-wave polarization in this direction (crossline) than perpendicular (inline). Many studies show that horizontal component data are valuable when steeply dipping structures are present (e.g., Purnell 1992; Stewart *et al.* 2003), which seems to be the case in our study. We expect the large velocity contrast (Table 1), the source used in this study, and layered structures as favorable for mode conversions (e.g., Lash 1982; Edelman 1985; Malehmir *et al.* 2009; Malinowski and White 2011; Bellefleur *et al.* 2004, 2012).

The S-wave signal (or P-S mode-conversion from it), however, appears to be generally too weak to image the basement. Alternatively, the processing approach is not ideal for the horizontal component data to image the basement. Based on Thomsen (1999), our estimation of P-wave and S-wave velocities from the first arrivals (ratio between 2 and 3), a maximum offset of 160 m (streamer length), and a maximum target depth of 100 m, we can expect the common midpoint binning approach to not suffer significantly, and only little smearing would occur. The NMO velocity correction would likely work at these offsets, particularly for

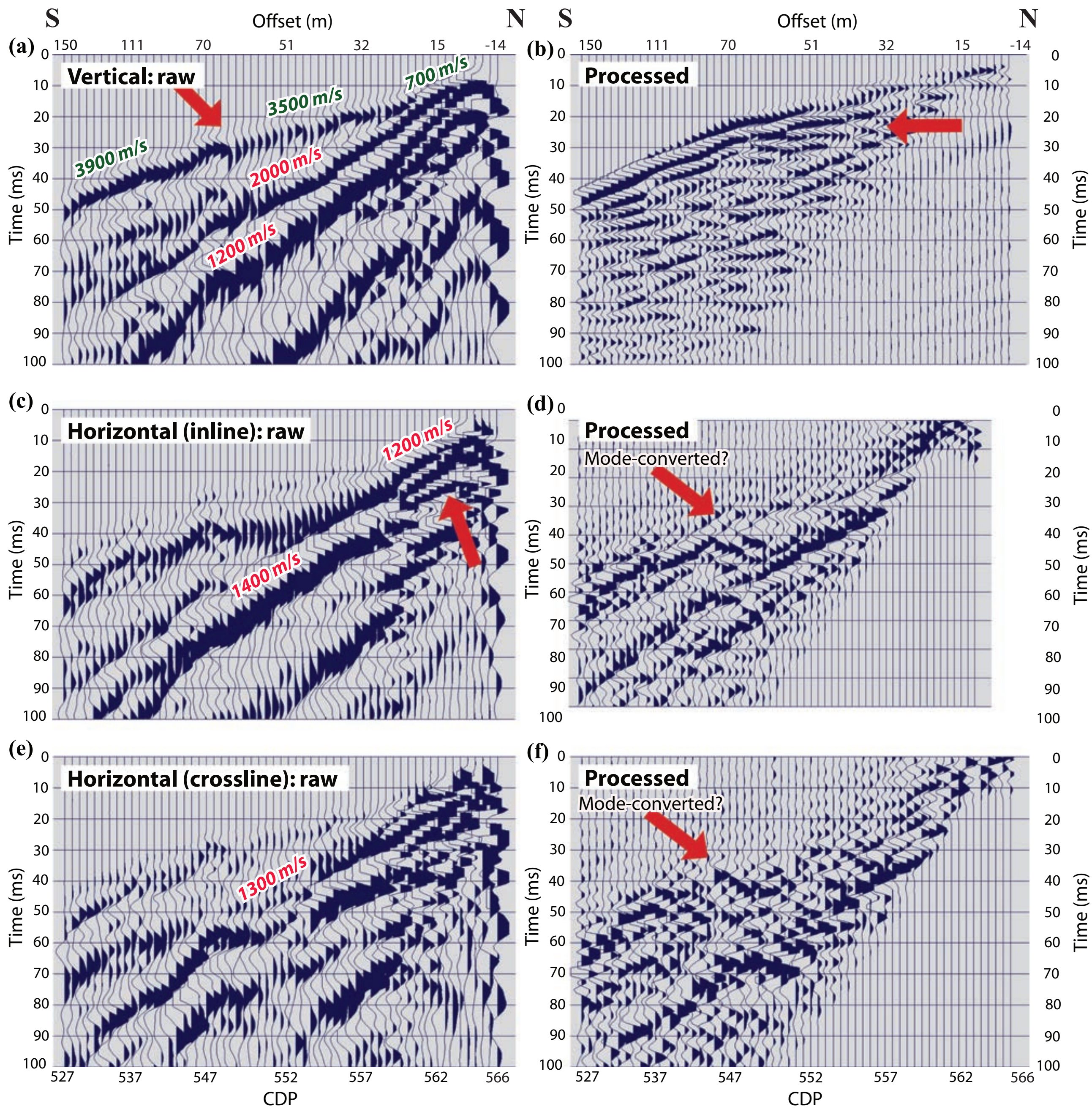

Figure 12 A shot gather recorded near the location of the magnetic lineament showing (a and b) raw and processed vertical component (c and d) raw and processed horizontal inline and (e and f) raw and processed horizontal crossline components of the data. A careful inspection of these data allows the verification of the steeply dipping reflection observed in the horizontal component data (e.g., Fig. 11c). Vertical component data show a sudden increase in the first arrival velocities towards the south and short reflections in horizontal inline and crossline component data (see the red arrows).

horizontal reflections and these depth ranges, at least down to the basement depth (~50 m depth). However, beyond this depth, common conversion point binning is more appropriate (Stewart *et al.* 2002, 2003). Future seismic studies should aim at providing a suitable shear-wave source and an approach to tackle the processing of these kinds of data and also further investigate the anisotropy signatures in the 3C data.

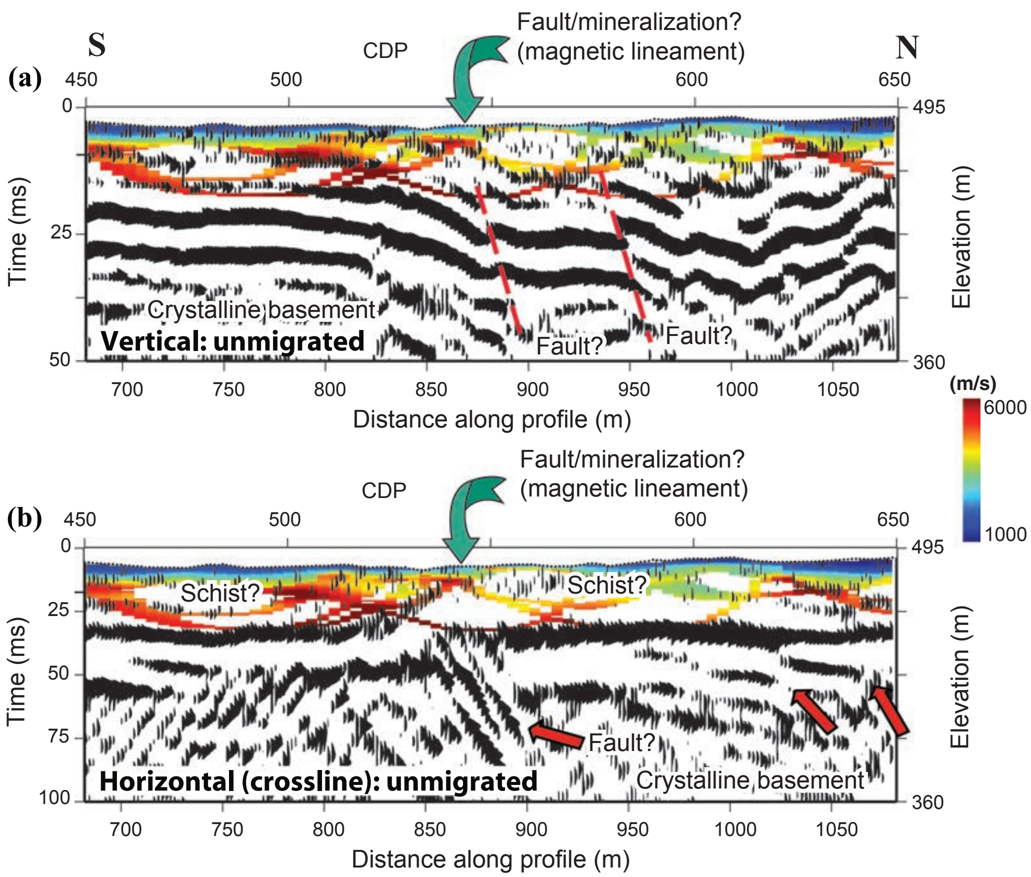

Figure 13 A portion of the P-wave first arrival tomographic result (Fig. 9b) superimposed on the unmigrated seismic sections of (a) vertical and (b) horizontal crossline components, respectively. A careful comparison between these data suggests disturbed velocities in the vicinity of where the magnetic lineament is observed and further supports our interpretation of a fault system at this location. Note that CDP and receiver elevations are different and that the superimposition is slightly approximate in the vertical direction.

The P-wave energy from the sledgehammer is likely too weak to generate significant mode conversions and thus is not suitable for 3C data acquisition (unless different arrangements e.g., wedged-shaped plates, are considered) in the study area. However, the source provided sufficient P-wave energy to image the crystalline basement down to a depth of about 90 m, which is quite promising. Due to the short sensor and source spacing, we argue that the high-fold data were important to increase the signal-to-noise ratio and that, if the sledgehammer data had been acquired at every 10 m instead, such as the explosive data, we would have had difficulties in imaging the basement. We also inspected the quality of the sledgehammer shots carefully and noticed that, depending on the ground conditions, the basement reflection had a different appearance in different source gathers. Figure 14 shows two-example sledgehammer source gathers (only vertical component shown). The basement reflection (marked by red arrows) is clear in both shot gathers. While these shots verify the presence of the reflection shown in Figure 10, it also clearly illustrates the variable frequency content of the sledgehammer data. The reflection observed in Figure 14a arrives only 10 ms later than the one observed in Figure 14b (based on their apexes). Nevertheless, the frequency content of the reflection and the data are nearly twice as in Figure 14a. This demonstrates the effect of the near-surface conditions on the sledgehammer data, which was not as noticeable in the explosive data. Future surveys will use a designated plate (e.g., wedged shape) for generating S-wave data. This was not attempted in this survey.

Linear magnetic anomalies and their relationships with the structures controlling the mineralization have been a matter of discussion in the study area. The working hypothesis is that the fault zones provide pathways for hydrothermal fluids, and these fluids get trapped within the sedimentary beds

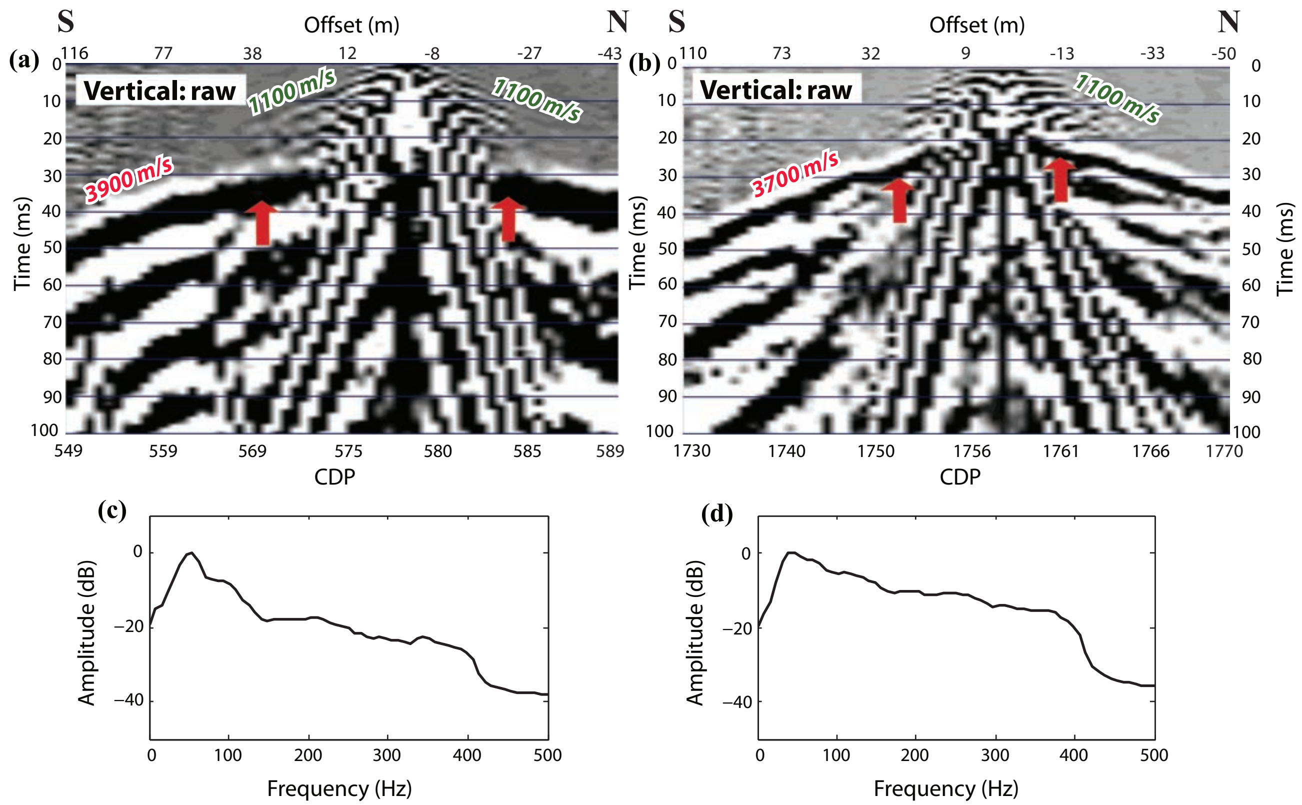

Figure 14 Two different source gathers, vertical component data, showing (a) a basement reflection at about 30 ms and (b) another one at about 20 ms time. These two reflections and their source records have different frequency content (spectra are shown for a window between 0 ms and 100 ms) as illustrated in (c and d). We relate this to different near-surface conditions at these source locations. CDP numbers correspond to those shown in Figure 10.

(and pores) that onlap basement highs (low porosity or impermeable); thus these anomalies, i.e., basement highs, are interesting from the exploration point of view (Lucks 2003; Casanova 2010; Saintilan *et al.* 2015).

Although there is no clear way to distinguish the cause of the magnetic anomaly (mafic dykes, basement high, or a fault) from airborne magnetic data alone, this study suggests that the magnetic lineament in the study area is associated with faulted structures and unlikely from dykes in the basement. However, it is not immediately clear why a fault should generate a magnetic signature in this environment unless it is associated with magnetic minerals. Thus, we argue that, although the magnetic lineaments are from fault systems, they are likely to be associated with local enrichment of magnetite in the host rock. A recent study by Saintilan *et al.* (2015) has suggested that the faults, most of them originally normal, were reactivated as reverse faults with upthrows between 5 m and 30 m, bringing mineral-bearing fluids to precipitate within the sandstones and the Alum Shale as caprock. In this scenario, one would expect magnetic minerals to lose their magnetic signature, and the faults rather become nonmagnetic.

A follow-up study with special attention to basement intersections in existing boreholes was undertaken to determine if the magnetic lineaments away from the seismic line could provide some complementary information. One borehole, BH25 (Fig. 2b), intersects the magnetic lineament anomaly about 1.5 km away from the seismic section. While in most other boreholes, the basement is a rather undeformed syenite, the first 5 m of the basement in BH25 is gneissic, gradually grading into fresh syenite. A handheld magnetic susceptibility metres showed consistently higher values (Table 1) for the gneiss than for the basement syenites in the surrounding boreholes. Notable heterogeneity in susceptibility in the fresh syenites was also present. The presence of gneiss can explain the positive magnetic lineament anomaly if we interpret its presence as a product of ductile shearing. Structurally, a deformed rock between coherent basement rocks represents a weak zone that can experience later brittle deformation/faulting and

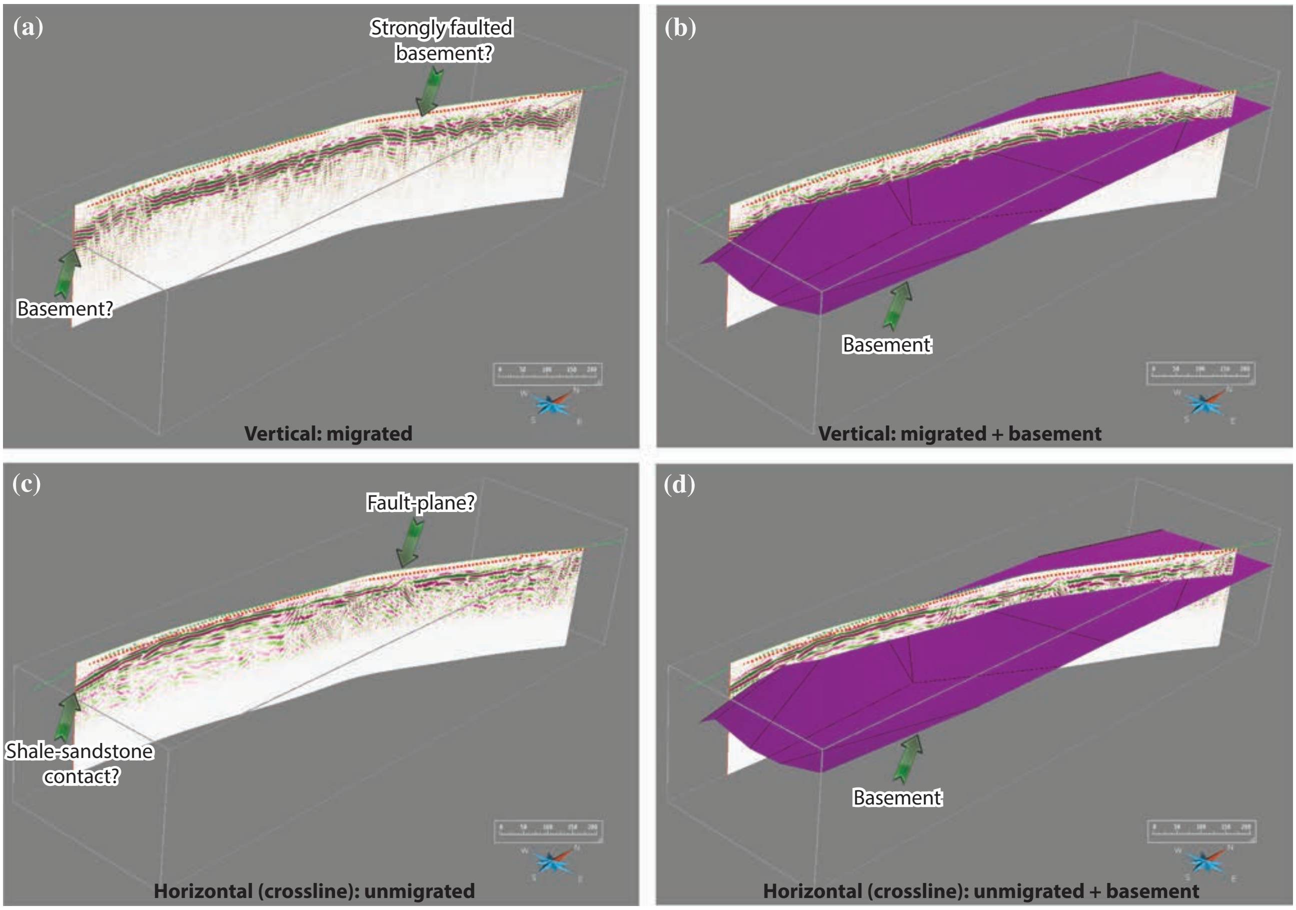

Figure 15 3D visualization of the seismic results showing (a and b) vertical component data and their correlation with a basement surface created by interpolation of available borehole data (Fig. 2), and (c and d) horizontal crossline component data and their correlation with the interpolated basement surface. Note that the reflection in the vertical component data better matches the basement surface than those in the crossline component data.

extensive erosion as well, which is likely imaged in the seismic data as displacement in the overlying sediments and erosional depressions in the basement. The mineralizing fluids would then be concentrated in the faults or basement depressions. Further ground magnetic and gravity measurements would be required to narrow down the size of the magnetic lineament to see if this is limited to only a 5 m-wide shear fabric zone or a wider zone comprising several of them.

Figure 15 shows a 3D visualization of the seismic sections (explosive data) with a surface representing the top of the basement based on available borehole data (blue/white dots in Fig. 2a). No borehole intersects the seismic line; thus, a direct comparison with geological data collected at depth cannot be made. However, the 3D views illustrate why we interpret the reflection in the vertical component data to be from the top of the basement and not the one in the horizontal crossline component data. The basement surface does not completely match the reflection in the vertical component seismic section, implying that a simple linear interpolation between the boreholes is likely incorrect. Paleo-erosion and resulting paleotopography must also be taken into account when comparing the two.

8 CONCLUSIONS

A case study demonstrating the value of using multicomponent seismic data for mineral exploration is demonstrated in this paper. It illustrates the capability of our recently developed prototype 3C MEMs-based landstreamer data acquisition system and its potential for shallow mineral exploration. Explosives and geological structures appear to have generated usable mode-converted wave signals. Therefore, it is an advantage if the signals are also recorded on horizontal component receivers. Horizontal component data supported by radio-magnetotelluric measurements successfully image a shallow reflection likely generated at the contact between shale/schist and sandstone, a major fault zone, and indications of a few smaller ones within the sandstone where the magnetic lineament is observed. The horizontal component data do not image the crystalline basement, which is interpreted to be 20 m–30 m deeper than the reflection observed on them. The vertical component data, however, penetrate deeper and successfully imaged the top of the crystalline basement. It is likely that the mineralization is related to faulted structures at the site. Both explosive and sledgehammer sources were able to provide sufficient signal to image the basement and its undulating surface; however, the sledgehammer data did not contain useful shear-wave signal.

ACKNOWLEDGMENTS

The seismic study was carried out within the frame of Trust2.2-GeoInfra (http://trust-geoinfra.se) project sponsored by Formas (project number 252–2012–1907), BeFo, SBUF, Boliden, Skanska, SGU, FQM, and NGI. Boliden Mineral AB sponsored this particular test survey for which we are grateful. S. Wang and B. Brodic would like to thank Formas, BeFo, SBUF, and Skanska for funding their PhD studies. We would like to thank the graduate students and staff from the Geophysics Program of Uppsala University for taking part in the acquisition of the seismic and RMT data, and the development of the seismic landstreamer. We would also like to thank A. Pugin, U. Polom, L. Dynesius, and H. Palm for their fruitful discussion and contributions into the development of the landstreamer. gOcad Consortium and Paradigm are thanked for providing an academic license of gOcad for 3D visualization and interpretation of the data. GLOBE Claritas™ under license from the Institute of Geological and Nuclear Sciences Limited, Lower Hutt, New Zealand was used to process the seismic data. GMT from P. Wessel and W.H.F. Smith and gOcad was used to prepare some of the figures. We would like to thank A. Tryggvason for providing his *ps-tomo* tomography code. Critical comments and reviews by two anonymous reviewers and the associate editor helped to improve the quality of our work and interpretation of the 3C data for which we are grateful.

REFERENCES

Adam E., Perron G., Arnold G., Matthews L. and Milkereit B. 2003. 3D seismic imaging for VMS deposit exploration, Matagami, Quebec. In: *Hardrock Seismic Exploration* (eds D.W. Eaton, B. Mikereit and M.H. Salisbury), pp. 229–246. Society of Exploration Geophysicists, Tulsa, Oklahoma, USA.

Ahmadi O., Juhlin C., Malehmir A. and Munck M. 2013. High-resolution 2D seismic imaging and forward modeling of a polymetallic sulfide deposit at Garpenberg, Central Sweden. *Geophysics* **78**, B339–B350.

Bansal R. and Gaiser J. 2013. An introduction to this special section: applications and challenges in shear-wave exploration. *The Leading Edge* **32**, 1–12.

Bastani M. 2001. *EnviroMT – a new controlled source/radio magnetotelluric system*. PhD thesis, Uppsala University, Uppsala, Sweden.

Bastani M., Malehmir A., Ismail N., Pedersen L.B. and Hedjazi F. 2009. Delineating hydrothermal stockwork copper deposits using controlled-source and radio-magnetotelluric methods: A case study from northeast Iran. *Geophysics* **74**, B167–B181.

Bellefleur G., Malehmir A. and Müller C. 2012. Elastic finite-difference modeling of volcanic-hosted massive sulfide deposits: A case study from Half Mile Lake, New Brunswick, Canada. *Geophysics* **77**, WC25–WC36.

Bellefleur G., Müller C., Snyder D. and Matthews L. 2004. Downhole seismic imaging of a massive sulphide orebody with mode-converted waves, Halfmile Lake, New Brunswick, Canada. *Geophysics* **69**, 318−329.

Bjørlykke A. and Sangster D.F. 1981. An overview of sandstone-lead deposits and their relationships to red-bed copper and carbonate-hosted lead-zinc deposits. In: *Economic Geology 75th Anniversary*, pp. 179–213. The Economic Geology Publishing Company.

Bohlen T., Müller C. and Milkereit B. 2003. Elastic wave scattering from massive sulfide orebodies: on the role of composition and shape. In: *Hardrock Seismic Exploration* (eds B. Milkereit, D.W. Eaton,and M. Salisbury), pp. 70–89. Society of Exploration Geophysicists, Tulsa, Oklahoma, USA.

Brodic B., Malehmir C. and Juhlin C. 2014. *Multicomponent broadband seismic landstreamer for high-resolution imaging and characterization*. 16th Seismix International Symposium, Barcelona, Spain.

Brodic B., Malehmir C., Juhlin C. and Bastani M. 2015. Multicomponent broadband seismic landstreamer for high-resolution imaging and site characterization. In preparation.

Casanova V. 2010. *Geological and geophysical characteristics of the Pb-Zn sandstone-hosted autochthonous Laisvall deposit in the perspective of regional exploration at the Swedish Caledonian Front*. MSc thesis. Luleå University of Technology, Luleå, Sweden.

Cheraghi S., Malehmir A. and Bellefleur G. 2012. 3D imaging challenges in steeply dipping mining environment: new lights on acquisition geometry and processing from the Brunswick No. 6 seismic data, Canada. *Geophysics* **77**, WC109–WC122.

Christofferson H.C., Wallin B., Selkman S. and Rickard D.T. 1979. Mineralization controls in the sandstone lead-zinc deposits at Vassbo, Sweden. *Economic Geology* **74**, 1239–1249.

Dehghannejad M., Juhlin C., Malehmir A., Skyttä P. and Weihed P. 2010. Reflection seismic imaging of the upper crust in the Kristineberg mining area, northern Sweden. *Journal of Applied Geophysics* **71**,125–36.

Dehghannejad M., Malehmir A., Juhlin C. and Skyttä P. 2012. 3D constraints and finite-difference modeling of massive sulfide deposits: The Kristineberg seismic lines revisited, northern Sweden. *Geophysics* **77**, WC69–WC79.

Duff D., Hurich C. and Deemer S. 2012. Seismic properties of the Voisey's Bay massive sulfide deposit: insights into approaches to seismic imaging. *Geophysics* **77**, WC59–WC68.

Eaton D.W. 1999. Weak elastic-wave scattering from massive sulfide ore bodies. *Geophysics* **64**, 289−299.

Eaton D.W., Adam E., Milkereit B., Salisbury M., Roberts B., *et al*. 2010. Enhancing base-metal exploration with seismic imaging. *Canadian Journal of Earth Sciences* **47**, 741−760.

Edelmann H.A.K. 1985. Shear-wave energy source. In: *Seismic Shear Waves, Part B: Applications* (ed G. Dohr), pp. 134–177. Geophysical Press.

Ehsan S.A., Malehmir A. and Dehghannejad M. 2012. Re-processing and interpretation of 2D seismic data from the Kristineberg mining area, northern Sweden. *Journal of Applied Geophysics* **80**, 43−55.

Garotta R. 2000. Shear waves from acquisition to interpretation. In: *Distinguished Instructor Series* **3**, Society of Exploration Geophysicists, Tulsa, Oklahoma, USA.

Gee D.G. 1975. A tectonic model for the central part of the Scandinavian Caledonides. *American Journal of Science* **275**, 468–515.

Gee D.G., Juhlin C., Pascal C. and Robinson P. 2010. Collisional Orogeny in the Scandinavian Caledonides (COSC). *GFF* **132**, 29–44.

Gillot E., Gibson M., Verneau D. and Laroche S. 2005. Application of high-resolution 3D seismic to mine planning in shallow platinum mines. *First Break* **23**, 59–64.

Greenhalgh S.A., Zhou B. and Cao S. 2003. A crosswell seismic experiment for nickel sulphide mineralization. *Journal of Applied Geophysics* **53**, 77–89.

Hajnal Z., White D., Takacs E., Gyorfi S., Annesley I.R., Wood G. *et al*. 2010. Application of modern 2D and 3D seismic reflection techniques for uranium exploration in the Athabasca Basin, in Lithoprobe: parameters, processes and the evolution of a continent. *Canadian Journal of Earth Sciences* **47**, 761−782.

Hedin P., Juhlin C. and Gee D.G. 2012. Seismic imaging of the Scandinavian Caledonides to define ICDP drilling sites. *Tectonophysics* 554–447, 30−41.

Hedin P., Malehmir A., Gee D., Juhlin C. and Dyrelius D. 2014. 3D interpretation by integrating seismic and potential field data in the vicinity of the proposed COSC-1 drill site, central Swedish Caledonides. In: *New Perspectives on the Caledonides of Scandinavia and Related Areas* (eds F. Corfu, D. Gasser and D.M. Chew), pp. 301–319. Geological Society, London, Special Publications.

Hole J.A. 1992. Nonlinear high-resolution three-dimensional seismic traveltime tomography. *Journal of Geophysical Research* **97**, 6553–6562.

Hurich C.A., Palm H., Dyrelius D. and Kristoffersen Y. 1989. Deformation of the Baltic continental crust during Caledonide intracontinental subduction: views from seismic reflection data. *Geology* **17**, 423–425.

Hurich C. and Deemer S. 2013. Combined surface and borehole seismic imaging in a hard rock terrain: a field test of seismic interferometry and virtual source profiling. *Geophysics* **78**, B103–B110.

Inazaki T. 2012. Delineation of detailed structure in Holocene unconsolidated sediments using S-wave type Land Streamer. *Proceedings of 74th EAGE Conference & Exhibition*, Copenhagen, Denmark, 2012, pp. 1–5.

Juhojuntti N., Juhlin C. and Dyrelius D. 2001. Crustal reflectivity underneath the Central Scandinavian Caledonides. *Tectonophysics* **334**, 191–210.

Juhojuntti N., Wood G., Juhlin C., O'Dowd C., Dueck P. and Cosma C. 2012. 3D seismic survey at the Millennium uranium deposit, Saskatchewan, Canada: mapping depth to basement and imaging post-Athabasca structure near the ore body. *Geophysics* **77**, WC245−WC258.

Kalscheuer T., Bastani M., Donohue S., Persson L., Pfaffhuber A.A., Reiser F. *et al*. 2013. Delineation of a quick clay zone at Smorgrav, Norway, with electromagnetic methods under geotechnical constraints. *Journal of Applied Geophysics* **92**, 121–136.

Koivisto E., Malehmir A., Heikkinen P., Heinonen S. and Kukkonen I. 2012. 2D reflection seismic investigations in the Kevitsa Ni-Cu-PGE deposit, northern Finland. *Geophysics* **77**, WC149–WC162.

Korja T., Smirnov M., Pedersen L.B. and Gharibi M. 2008. Structure of the Central Scandinavian Caledonides and the underlying Precambrian basement, new constraints from magnetotellurics. *Geophysical Journal International* **175**, 55–69.

Krawczyk C.M., Polom U., Trabs S. and Dahm T. 2012. Sinkholes in the city of Hamburg—New urban shear-wave reflection seismic system enables high-resolution imaging of sub-erosion structures. *Journal of Applied Geophysics* **78**, 133–143.

Lash C.C. 1982. Investigation of multiple reflections and wave conversion by means of a vertical wave test (vertical seismic profiling) in southern Mississippi. *Geophysics* **47**, 977–1000.

Lilljequist R. 1973. Caledonian geology of the Laisvall Area, southern Norrbotten, Swedish Lapland. *Sveriges geologiska undersökning Serie C* **691**, 43.

Malehmir A. and Bellefleur G. 2009. 3D seismic reflection imaging of volcanic-hosted massive sulfide deposits: insights from reprocessing Halfmile Lake data, New Brunswick, Canada. *Geophysics* **74**, B209–B219.

Malehmir A., Schmelzbach C., Bongajum E., Bellefleur G., Juhlin C. and Tryggvason A. 2009. 3D constraints on a possible deep > 2.5 km massive sulphide mineralization from 2D crooked-line seismic reflection data in the Kristineberg mining area, northern Sweden. *Tectonophysics* **479**, 223–240.

Malehmir A., Dahlin P., Lundberg E., Juhlin C., Sjöström H. and Högdahl K. 2011. Reflection seismic investigations in the Dannemora area, central Sweden: insights into the geometry of polyphase deformation zones and magnetite-skarn deposits. *Journal of Geophysical Research* **116**, B11307.

Malehmir A., Andersson M., Lebedev M., Urosevic M. and Mikhaltsevitch V. 2013a. Experimental estimation of velocities and anisotropy of a series of Swedish crystalline rocks and ores. *Geophysical Prospecting* **61**, 153–167.

Malehmir A., Bastani M., Krawzyck C., Gurk M., Ismail N., Polom U. *et al*. 2013b. Geophysical assessment and geotechnical investigation of quick-clay landslides – a Swedish case study. *Near Surface Geophysics* **11**, 341–350.

Malehmir A., Durrheim R., Bellefleur G., Urosevic M., Juhlin C., White D. *et al.* 2012a. Seismic methods in mineral exploration and mine planning: a general overview of past and present case histories and a look into the future. *Geophysics* 77, WC173–WC190.

Malehmir A., Koivisto E., Manzi M., Cheraghi S., Durrheim R., Bellefleur G. *et al.* 2014. A review of reflection seismic investigations in three major metallogenic regions: the Kevitsa Ni-Cu-PGE district (Finland), Witwatersrand goldfields (South Africa), and the Bathurst Mining Camp (Canada). *Ore Geology Reviews* **56**, 423–441.

Malehmir A., Juhlin C., Wijns C., Urosevic M., Valasti P. and Koivisto E. 2012b. 3D reflection seismic investigation for open-pit mine planning and exploration in the Kevitsa Ni-Cu-PGE deposit, Northern Finland. *Geophysics* 77, WC95–WC108.

Malinowski M. and White D. 2011. Converted wave seismic imaging in the Flin Flon mining camp. *Journal of Applied Geophysics* **75**, 719–730.

Malinowski M., Schetselaar E. and White D. 2012. 3D seismic imaging in the Flin Flon VMS mining camp – Part II: Forward modeling. *Geophysics* **77**, WC81–WC93.

Manzi M.S.D., Gibson M.A.S., Hein K.A.A., King N. and Durrheim R.J. 2012a. Application of 3D seismic techniques in evaluation of ore resources in the West Wits Line goldfield and portions of the West Rand Goldfield, South Africa. *Geophysics* **77**, WC163–WC171.

Manzi M., Durrheim R.J., Hein K.A.A. and King N. 2012b. 3D edge detection seismic attributes used to map potential conduits for water and methane in deep gold mines in the Witwatersrand basin, South Africa. *Geophysics* **77**, WC133–WC147.

Milkereit B., Berrer E.K., King A.R., Watts A.H., Roberts B., Adam E. *et al.* 2000. Development of 3−D seismic exploration technology for deep nickel-copper deposits-A case history from the Sudbury basin, Canada. *Geophysics* **65**, 1890−1899.

Milkereit B., Eaton D.W., Wu J., Perron G., Salisbury M.H., Berrer E. *et al.* 1996. Seismic imaging of massive sulphide deposits: Part II. Reflection seismic profiling. *Economic Geology* **91**, 829−834.

Pedersen L.B. and Engels M. 2005. Routine 2D inversion of magnetotelluric data using the determinant of the impedance tensor. *Geophysics* **70**, 31−41.

Podvin P. and Lecomte I. 1991. Finite difference computation of traveltimes in very contrasted velocity models: a massively parallel approach and its associated tools. *Geophysical Journal International* **105**, 271–284.

Polom U., Hansen L., Sauvin G., L'Heureux J.-S., Lecomte I., Krawczyk C.M. *et al.* 2010. High-resolution SH-wave seismic refl ection for characterization of onshore ground conditions in the Trondheim harbor, central Norway. In: *SEG Geophysical Developments Series No. 15: Advances in Near-Surface Seismology and Ground-Penetrating Radar* (eds R.D. Miller, J.D. Bradford, and K. Holliger), pp. 75–92. Society of Exploration Geophysicists, Tulsa, Oklahoma, USA.

Pretorius C.C., Trewick W.F., Fourie A. and Irons C. 2000. Application of 3D seismics to mine planning at Vaal Reefs Gold Mine, number 10 shaft, Republic of South Africa. *Geophysics* **65**, 1862−1870.

Pugin A.J.-M., Pullan S.E. and Hunter J.A. 2010. Update on recent observations in multicomponent seismic reflection profiling. 23rd EEGS Symposium on the Application of Geophysics to Engineering and Environmental Problems.

Pugin A.J.-M., Brewer K., Cartwright T., Pullan S.E., Perret D., Crow H. *et al.* 2013. Near surface S-wave seismic reflection profiling—new approaches and insights. *First Break* **31**, 49–60.

Purnell G.W. 1992. Imaging beneath a high-velocity layer using converted waves. *Geophysics* **57**, 1444–1452.

Rasmussen T., Roberts R. and Pedersen L. 1987. Magnetotellurics along the Fennoscandian long range profile. *Geophysical Journal of the Royal Astronomical Society* **89**, 799–820.

Rickard D.T., Willdén M.Y., Marinder N.E. and Donnelly T.H. 1979. Studies on the genesis of the Laisvall sandstone lead-zinc deposit, Sweden. *Economic Geology* **74**, 1255−1285.

Romer R. 1992. Sandstone-hosted lead-zinc mineral deposits and their relation to the tectonic mobilization of the Baltic Shield during the Caledonian orogeny, a reinterpretation. *Mineralogy and Petrology* **47**, 67−85.

Saintilan N.J.D., Fontboté L., Stephens M.B. and Lundstam E. 2013. Reactivated basement structures and their control on sandstone-hosted Pb-Zn deposit along the eastern front of the Scandinavian Caledonides. *Proceedings of the 12th Society for Geology Applied to Mineral Deposits Biennial Meeting* **4**, 1667–1670.

Saintilan N.J.D., Stephens M.B., Lundstam E. and Fontboté L. 2015. Control of reactivated Proterozoic basement structures on sandstone-hosted Pb-Zn deposits along the Caledonian Front, Sweden: evidence from airborne magnetic data, structural analysis, and ore-grade modeling. *Economic Geology* **110**, In press.

Salisbury M.H., Harvey C.W. and Matthews L. 2003. The acoustic properties of ores and host rocks in hardrock terranes. In: *Hard Rock Seismic Exploration* (eds D.W. Eaton, B. Mikereit and M.H. Salisbury), pp. 9–19. Society of Exploration Geophysicists.

Schmusker U. 1970. An introduction to induction anomalies. *Journal of Geomagnetism and Geoelectricity* **22**, 9−33.

Shan C., Bastani M., Malehmir A., Persson L. and Engdahl M. 2014. Integrated 2D modeling and interpretation of geophysical and geotechnical data to delineate quick clays at a landslide site in southwest Sweden. *Geophysics* **79**, EN61–EN75.

Snyder D.B., Cary P. and Salisbury M. 2008. 2D−3C high-resolution seismic data from the Abitibi Greenstone Belt, Canada. *Tectonophysics* **472**, 226–237.

Soper N.J., Strachan R.A., Holdsworth R.E., Gayer R.A. and Greiling R.O. 1992. Sinistral transpression and the Silurian closure of Iapetus. *Journal of the Geological Society* **149**, 871–880.

Speis B.R. 1989. Depth of investigation in electromagnetic sounding methods. *Geophysics* **54**, 872–888.

Stephens M.B. and Gee D.G. 1985. A tectonical model for the evolution of the eugeoclinal terranes in the central Scandinavian Caledonides. In: *The Caledonian Orogen—Scandinavia and Related Areas* (eds D.G. Gee and B.A. Sturt), pp. 953–978. John Wiley, Chichester, England.

Stewart R.R., Gaiser J.E., Brown R.J. and Lawton D.C. 2002. Converted-wave seismic exploration: methods. *Geophysics* **67**, 1348–1363.

Stewart R.R., Gaiser J.E., Brown R.J., and Lawton D.C. 2003. Converted-wave seismic exploration: applications. *Geophysics* **68**, 40–57.

Tessmer G. and Behle A. 1988. Common reflection point data stacking technique for converted waves. *Geophysical Prospecting* **36**, 671–688.

Thomsen L. 1999. Converted-wave reflection seismology over inhomogeneous, anisotropic media. *Geophysics* **64**, 678–690.

Tryggvason A., Rögnvaldsson S.T. and Flovenz Ó.G. 2002. Three dimensional imaging of P- and S-wave velocity structure and earthquake locations beneath southwest Iceland. *Geophysical Journal International* **151**, 848–866.

Urocevic M., Ganesh B. and Marcos G. 2012. Targeting nickel sulphide deposits from 3D seismic reflection data at Kambalda, Australia. *Geophysics* 77, WC123−WC132.

Welin E. 1970. Den svekofenniska orogena zonen i norra Sverige – En preliminär diskussion. *GFF* **92**, 433–451.

White D., Boerner D., Wu J., Lucas S., Berrer E., Hannila J. *et al.* 2000. Mineral exploration in the Thompson nickel belt, Manitoba, Canada, using seismic and controlled-source EM methods. *Geophysics* **65**, 1871−1881.

White D.J., Secord D. and Malinowski M. 2012. 3D seismic imaging in the Flin Flon VMS mining camp: part I — seismic results. *Geophysics* 77, WC47–WC58.

Willdén M. 2004. The Laisvall sandstone-hosted Pb-Zn deposit: geological overview. In: *Society of Economic Geologists, Guidebook Series* **33**, pp. 115−127.